

Catalytic activation of ethylene C-H bonds on uniform d⁸ Ir(I) and Ni(II) cations in zeolites: toward molecular level understanding of ethylene polymerization on heterogeneous catalysts

Nicholas R. Jaegers^{1,2,&,*}, Konstantin Khivantsev^{1,&,*}, Libor Kovarik¹ Daniel W. Klas¹, Jian Zhi Hu¹, Yong Wang^{1,2}, and János Szanyi^{1,&,*}

¹Institute for Integrated Catalysis, Pacific Northwest National Laboratory Richland, WA 99352 USA

²Voiland School of Chemical Engineering and Bioengineering, Washington State University, Pullman, WA 99163 USA

& These authors contributed equally

*corresponding authors: Nicholas.Jaegers@pnnl.gov, Konstantin.Khivantsev@pnnl.gov, Janos.Szanyi@pnnl.gov

ABSTRACT: The homolytic activation of the strong C-H bonds in ethylene is demonstrated, for the first time, on d⁸ Ir(I) and Ni(II) single atoms in the cationic positions of zeolites H-FAU and H-BEA under ambient conditions. The oxidative addition of C₂H₄ to the metal center occurs with the formation of a d⁶ metal vinyl hydride, explaining the initiation of the Cossee-Arlman cycle on d⁸ M(I/II) sites in the absence of pre-existing M-H bonds. Under mild reaction conditions (80-220°C, 1 bar), the catalytic dimerization to butenes and dehydrogenative coupling of ethylene to butadiene occurs over these catalysts. Butene-1 is not converted to butadiene under the reaction conditions applied. Post-reaction characterization of the two materials reveals that the active metal cations remain site-isolated whereas deactivation occurs due to the formation of carbonaceous deposits on the zeolites. Our findings have significant implications for the molecular level understanding of ethylene conversion and the development of new ways to functionalize C-H bonds under mild conditions.

Zeolite-supported transition metals (single atoms, clusters, nanoparticles, etc.) represent an important class of materials with uses in the chemical industry, emissions controls, and as model systems to derive structure-function properties in catalysis.¹⁻⁹ Among them, d⁸ metals such as Ni(II), Rh(I), Ir(I), Pt(II), and Pd(II) have been the focus of many studies to better understand the genesis, speciation, and stability of such species for reactions such as hydrogenations, oxidations, as well as ethylene transformation (dimerization and oligomerization to butenes and higher oligomers).¹⁰⁻¹³ For example, it was shown first in the 1950s that Rh(I)(CO)₂ and Ir(I)(CO)₂ species can be stabilized on oxide supports¹⁴⁻¹⁵ and are active for ethylene conversion to butenes at room temperature, retaining their site-isolated nature after catalysis.¹⁶⁻¹⁸

The Rh ligand environment is tunable and hydrogen promotes butene formation despite not directly participating in the dimerization reaction (i.e., 2C₂H₄ → C₄H₈).^{12, 17-18} This effect was explained in some studies by H₂ enhancing butene desorption on (Rh(C₂H₄)₂/HY).¹⁶ Recently, however, the hydrogen partial pressure dependence of ethylene dimerization was systematically measured on Rh(CO)₂, Rh(CO)(C₂H₄), Rh(CO)(H),¹⁷ and Rh(NO)₂¹² complexes supported on HY zeolites. Positive reaction orders of ~0.7-1 confirmed that hydrogen indeed promotes dimerization, where H₂ was shown to improve the rate of ethylene dimerization up to ~10 fold.^{12,17} This was attributed to the formation of metal-hydride-supported species (observed and characterized experimentally^{12,17,18}) which provide a low-energy pathway for dimerization via facile insertion of pi-coordinated ethylene into the M-H bond to form an M-Ethyl moiety which subsequently migrates into another pi-coordinated ethylene to form a

Rh-Butyl species prior to facile β-H abstraction to produce butene-1.¹² This attribution was subsequently supported for ethylene dimerization on Ni/BEA, although Ni-H species were not observed directly.¹⁹ Until now, it remained unclear how ethylene, in the absence of M-hydride species, can polymerize considering the importance of M-H intermediates in the Cossee-Arlman mechanism. Theoretical studies have identified potential mechanisms for ethylene dimerization on Ni/BEA where the metallocycle, proton-transfer, and Cossee-Arlman mechanisms were compared.²⁰ Also considered was the non-catalytic formation of a nickel vinyl intermediate via the heterolytic activation of a C-H bond over Ni(II)-O bond followed by the formation of an active Ni center.²⁰

In this study, we demonstrate the : 1). Preparation and characterization of highly uniform d⁸ metal species. Ni(II) was selected because it has been a challenge to prepare well-defined uniform Ni-zeolite species. We have previously prepared d⁸ Pt(II) and Pd(II) species⁹ in zeolite uniformly and thus transferred this approach to a Ni/BEA system in order to unravel detailed structure catalytic-property relationships for the historically important system for ethylene polymerization. We also employ the well-defined square planar d⁸ Ir(I)(CO)₂ complex anchored in zeolite FAU (like Ni(II)/FAU) because it grafts uniformly in zeolite and also has CO groups which, due to their high molar extinction coefficients and well-resolved nature, allow us to observe ligand changes with enhanced resolution. 2). We obtain the reactivity for ethylene couplings on those materials, showing similar trends for both d⁸ metals 3). We resolve a longstanding uncertainty in heterogeneous ethylene polymerization, one of the largest catalytic processes. Though supported metal ions (d⁸ like Ni(II), Ir(I), Pd(II) or d⁴ Cr(II) perform this reaction without the initiator/co-catalyst, the mechanism for ethylene polymerization initiation and the relevant intermediates involved have remained elusive for the last 50 years. We resolve these uncertainties using state-of-the-art infrared studies supported by microscopy and solid-state NMR measurements for d⁸ metal cations on solid supports. In short, ethylene polymerization starts with the homolytic activation of the C-H bonds of ethylene on extremely electrophilic d⁸ M sites, resulting in the formation of d⁶ metal vinyl hydride complexes which further react with ethylene to form a vinyl ethyl d⁶ metal fragment. From this fragment, butene-1 can form either via direct reductive elimination or a Cossee-Arlman type step involving alkyl chain growth through alkyl migration and insertion into M-ethylene bonds.

Though reported for other d⁸ metals, it is not straightforward to generate uniform Ni(II) species since they may graft to both silanol nests and various extra-framework zeolite positions, evidenced by IR spectroscopy of CO adsorption.¹⁹ This brought into question the true active center for ethylene oligomerization activ-

ity.²¹ To better understand the active centers for ethylene dimerization, well-defined supported complexes of Ir(I) and Ni(II) were generated, characterized, and tested in this study. These active centers not only demonstrate activity to butenes, but butadiene as well; a notable result since 1,3-butadiene is a high-value commodity chemical (~10 million tons per annum) that serves as a precursor to a wide range of plastics and polymers. These reactions proceed via activation of C-H bonds of ethylene on a super electrophilic cationic metal center recently observed for a metal/zeolite system.²²

A modified IWI method was previously used to produce atomically dispersed Pt and Pd in SSZ-13.⁹ We slightly altered this procedure to synthesize 0.4 wt% Ni on BEA by reacting aqueous nickel nitrate with excess ammonia to produce a mononuclear Ni hexamine complex. This mitigates the formation of hydroxo-bridged Ni complexes, which are precursors to NiO nanoparticles, similar to the aqueous solution of Pd(NO₃)₂ that has the propensity to darken and form ...-OH-Pd-OH-Pd-OH-... networks over time, even in acidic solutions.²³⁻²⁴ The micropores of BEA zeolite (Si/Al ~ 12.5) were impregnated with this complex, dried in ambient air, and calcined at 550°C in static air. Infrared spectroscopy of adsorbed CO on this material substantiates the exclusive formation of 1 type of Ni(II)-CO in BEA zeolite. The C-O stretching vibrational band of this species is located at 2,211 cm⁻¹ (Figure 1A).

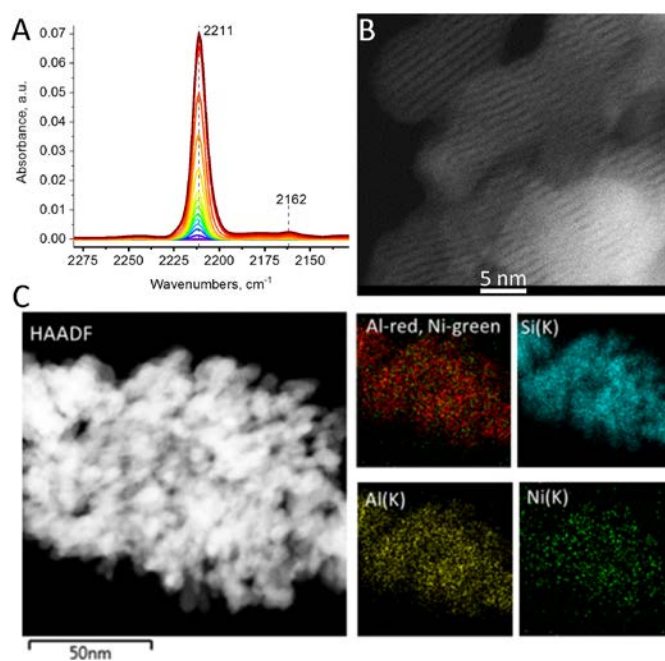


Figure 1. A). FTIR during CO adsorption on dry 0.4% Ni/BEA, $P(\text{CO})_{\text{max}}=5$ Torr (the band at 2162 cm⁻¹ represents adsorbed ¹³CO molecules) B). High-resolution HAADF-STEM image of the 0.4% Ni/BEA material: straight channels in BEA nanocrystals are clearly imaged. No NiO clusters or particles observed (additional HAADF-STEM images provided in Figure S2) C). EDS mapping of Ni, Al, Si, and Ni/Al overlay in 0.4% Ni/BEA.

No NiO clusters or nanoparticles could be observed in the channels of BEA. EDS mapping confirmed the presence of Ni associated with BEA, corroborating the presence of uniform, isolated Ni sites in the sample (Fig. 1B and C, Figure S1-S3). Comprehensive interconversion maps of Ni(II)-CO, Ni(II)-NO, Ni(II)-C₂H₄, and

Ni(II)(NO)(CO) complexes, never prepared through classical organometallic routes are discussed and available in the Supporting Information (Figure S4-S17). These provide new insight into the Ni/Zeolite chemistry complementary to the previous pioneering studies of Hadjiivanov et al.²⁵ In particular, a new phenomenon in solid supported systems is identified whereby low-temperature CO adsorption produces 2 peaks at 2,214 and 2,204 cm⁻¹ (Figure S11), that do not belong to the Ni(II)(CO)₂ dicarbonyl complex (evidenced by their contrasting interactions with C₂H₄ and stability under vacuum, Figs. S12, S13). However, CO adsorption at room temperature produces only 1 band at 2,211 cm⁻¹. This indicates that at low temperatures, distinctive Al T-sites exist while at room temperature these sites become degenerate, possibly due to the flexibility of the zeolite framework or relativistic effects, revealing only the 2,211 cm⁻¹ feature from CO adsorption on super electrophilic Ni(II)/2Al centers.

Unlike Rh(I)/FAU complexes, for which initial ligand environment impacts ethylene dimerization,^{12, 17-18} both Ni(II)-CO and Ni(II)-NO undergo ligand replacement by ethylene to form Ni(II)-C₂H₄ complex under ambient conditions and lower temperatures (Figure S5, S9, S13-S15). This material was active for ethylene transformation to butenes, demonstrating that Ni(II) in the ion-exchange position is active for catalysis (Table S1). Remarkably, 80°C was sufficient to observe activity for both butadiene as well as butenes (butene-1 as well as cis- and trans-2-butene) formation. Selectivity initially favored butadiene at 120°C (~65%, TOF ~122 hr⁻¹ with respect to butadiene formed and ~240 hr⁻¹ with respect to ethylene molecules reacted, Table S1), however, selectivity quickly dropped to ~10% within the first 30 minutes (TOF ~ 10 hr⁻¹). Above 180°C, activity for butadiene production is enhanced with selectivity around 20-30% on a molar basis at 200°C and initial TOF ~200 hr⁻¹. Even at elevated temperatures, deactivation is observed both for butene and butadiene production with time on stream (Figure S18).

These results are noteworthy since C-H bond activation in ethylene (22 kJ/mol stronger than methane at 298K) is a challenging catalytic step. Accordingly, functionalization of ethylene typically involves reactions with its C=C bond and not the C-H bond directly. By activating the C-H bond in ethylene, the formal coupling of two vinyl C₂H₃ fragments enables the formation of butadiene.

Catalytically, butadiene can be produced by dehydrogenation of n-butane and 1-butene (Houdry process) or by ethanol conversion to butadiene, hydrogen, and water over a mixed metal oxide catalyst (Lebedev and Ostromyslenski process). These catalytic processes with unpromoted catalysts produce butadiene unselectively and are energy intensive (400-700°C).²⁶ The best current processes based on ethanol show excellent selectivity to butadiene for promoted materials (>90%) whereas the unpromoted, historically important Ta-containing material has a selectivity of ~15%. However, this process relies on a low ethanol feed rate (GHSV), features turnovers of ~ 1 hr⁻¹ at 320°C, and suffers deactivation due to formation of polymeric carbonaceous deposits.²⁷⁻²⁸

Though pathways from alcohol feedstocks exist, the catalytic conversion of ethylene to butadiene remains effectively unprecedented with just a few examples proposed. In 1983, (C₅(CH₃)₅)₂Ti(C₂H₄) complexes in aromatic solvents were suggested to convert ethylene into 1,3-butadiene and ethane at 25°C and ~4 atm in a sealed batch reactor, though the reported TOF after one year was ~1-2 year⁻¹, rendering catalysis indeterminate.²⁹ Notably, in 2015 ethylene has been selectively converted to butadiene over FAU-supported Rh(CO)₂ and Rh(CO)(C₂H₄) single-atom catalysts at 25°C and 1 atm under continuous ethylene flow,

yielding a TOF of $\sim 2 \text{ hr}^{-1}$,¹⁷ marking the discovery of the dehydrogenative coupling of ethylene into butadiene ($2\text{C}_2\text{H}_4 \rightarrow \text{C}_4\text{H}_6 + \text{H}_2$). In 2018, an $\text{Ir}(\text{C}_2\text{H}_4)_2(\text{Phebox})$ organometallic complex was shown to convert ethylene catalytically via $3\text{C}_2\text{H}_4 \rightarrow \text{C}_4\text{H}_6 + \text{C}_2\text{H}_6$ with butene by-products [$\text{S}_{\text{C}_4\text{H}_6} < 45\%$; P: 2-12 atm; TOF: 0.25 hr^{-1} at 2 atm/ 100°C , 0.9 hr^{-1} at 12 atm/ 110°C].³⁰ Despite this progress, the catalytic chemistry of butadiene formation from a cheap ethylene feedstock under mild conditions remains unattained, demonstrating the relevance of the observed butadiene activity at 120°C for Ni/BEA. We note that fast deactivation at this temperature is not surprising considering that H-zeolites are often used as butadiene adsorbents.³⁹

After catalysis, exposure of the sample to CO restores the original $2,211 \text{ cm}^{-1}$ feature (Figure S16-S17), but to a lesser extent due to unsaturated carbonaceous deposits blocking the active sites, further confirmed by *in situ* ^{13}C NMR (Figure S24).³¹ The absence of vibrational signatures for Ni(I) and Ni(0) carbonyl complexes further suggests that no reduction of Ni(II) occurred during ethylene dimerization and that Ni(II) in the ion-exchange positions of the zeolite is the active site in ethylene dimerization (Figure S17).

Moreover, post-reaction (200°C in ethylene flow) CO adsorption reveals a peak around $\sim 2,230 \text{ cm}^{-1}$ (Figure S16-17) not present in the fresh sample. This corresponds to CO adsorbed on extraframework aluminium⁴⁰ formed under mild catalytic conditions in the presence of Ni(II) atoms and ethylene. Solid-state NMR further confirms this result via comparison of ^{27}Al MAS NMR spectra of fresh and spent samples (Figure S19) which show that dealumination indeed occurs under mild conditions, evidenced by a feature at $\sim 30 \text{ ppm}$ due to the presence of penta-coordinate extraframework Al sites as well as broadening of tetrahedral Al bands. Such mild conditions have been not previously reported to cause dealumination of the zeolite framework. This is likely due to polymerization of ethylene in the microporous channels and the subsequent breakage of pores.

In addition to the supported d^8 Ni(II) species, a 0.7 wt% $\text{Ir}(\text{CO})_2$ species was prepared on H-FAU zeolite with Si/Al ~ 15 as for Ni/BEA. This formulation was previously characterized with EXAFS and FTIR,³² where its interaction with ethylene was reported to produce $\text{Ir}(\text{CO})(\text{C}_2\text{H}_4)$ complexes. Pulses of ethylene, followed by inert gas purging indeed produce only the $\text{Ir}(\text{CO})(\text{C}_2\text{H}_4)$ complex in this study (Figure 2A,C).

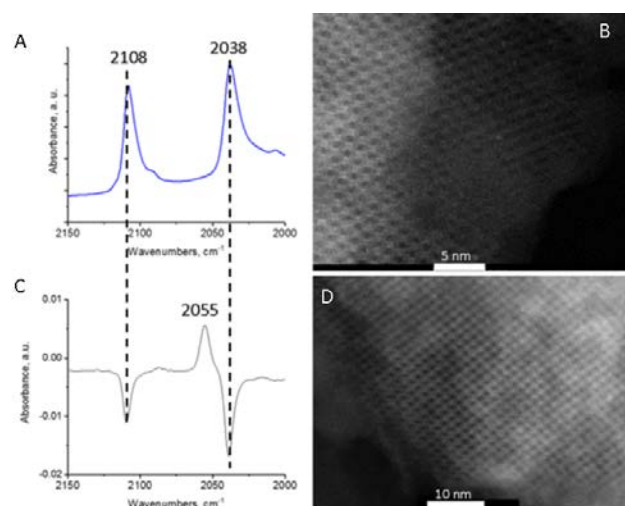


Figure 2. A). DRIFTS spectrum of the starting 0.7% $\text{Ir}(\text{CO})_2/\text{FAU}$ Si/Al ~ 15 material B). High-resolution HAADF-STEM image of the fresh Ir/FAU in [110] projection, individual Ir atoms can be seen in the supercells C). DRIFTS difference spectrum during reaction of $\text{Ir}(\text{CO})_2/\text{FAU}$ with pulses of dilute ethylene, showing disappearance of $2,108$ and $2,038 \text{ cm}^{-1}$ bands of $\text{Ir}(\text{CO})_2$ and appearance of only 1 new band at $2,055 \text{ cm}^{-1}$, belonging to $\text{Ir}(\text{CO})(\text{C}_2\text{H}_4)/\text{FAU}$ complex. D). High-resolution HAADF-STEM image of $\text{Ir}(\text{CO})_2/\text{FAU}$ after ethylene catalysis at 225°C for 1 hour, in the [110] projection, showing lack of Ir agglomeration.

DRIFTS confirms the successful grafting of the complex with the formation of symmetric and asymmetric CO stretches of the square-planar $\text{Ir}(\text{CO})_2$ fragment at $2,108$ and $2,038 \text{ cm}^{-1}$.^{12,17,18} HAADF-STEM imaging (Figure S20, 2B) further confirms site-isolated nature of the complex in the zeolite micropores. Sample exposure to flowing pure C_2H_4 in the DRIFTS cell revealed transient behavior (Figure 3).

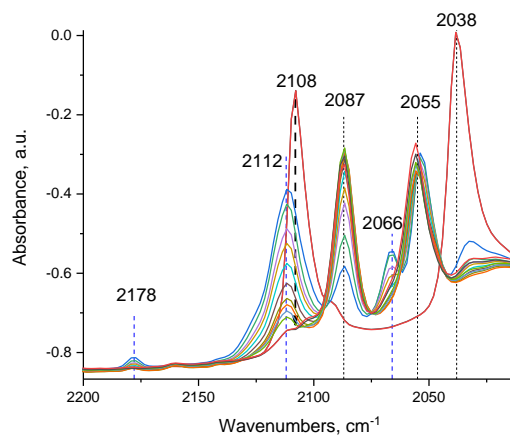
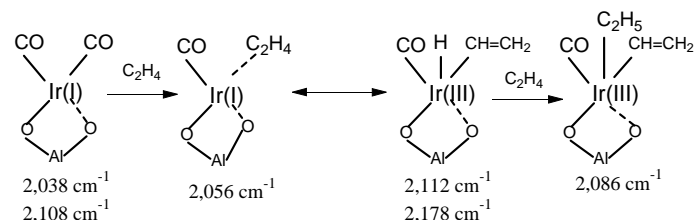


Figure 3. DRIFTS spectrum of 0.7% $\text{Ir}(\text{CO})_2/\text{FAU}$ Si/Al ~ 15 during exposure to flowing pure ethylene (the first 5 minutes).



The peaks, belonging to the symmetric and asymmetric CO stretches of $\text{Ir}(\text{CO})_2$, at $2,108$ and $2,038 \text{ cm}^{-1}$ declined while new features emerged. The $2,055 \text{ cm}^{-1}$ feature has been previously assigned to the $\text{Ir}(\text{CO})(\text{C}_2\text{H}_4)$ complex^{12,17,18}, however, careful inspection of the spectra in the $2,060 - 2,030 \text{ cm}^{-1}$ region reveals new features (Figure 4): the $2,066$ and $2,053 \text{ cm}^{-1}$ peaks decrease in concert as the $2,056 \text{ cm}^{-1}$ feature of $\text{Ir}(\text{CO})(\text{C}_2\text{H}_4)$ grows with clear isosbestic points (shaded).

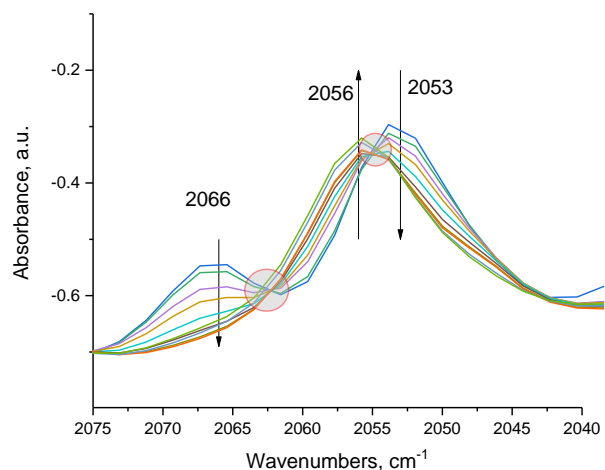
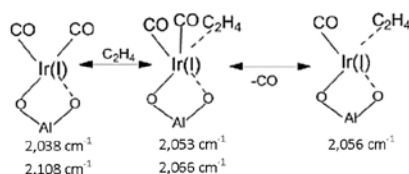


Figure 4. DRIFTS spectrum of 0.7% Ir(CO)₂/FAU Si/Al~15 during exposure to flowing ethylene (initial 5 minutes).

This indicates the stoichiometric transformation of Ir(CO)₂ into Ir(CO)(C₂H₄), occurring via the following sequence:



Initially, the square-planar Ir(CO)₂ accepts one C₂H₄ ligand to form a Ir(CO)₂(C₂H₄) species which then expels one CO ligand, forming square-planar Ir(CO)(C₂H₄). Concomitantly bands at 2,178 cm⁻¹ (weak) and 2,112 cm⁻¹ (intense) develop within the first 1 minute of ethylene exposure (Figure 5).

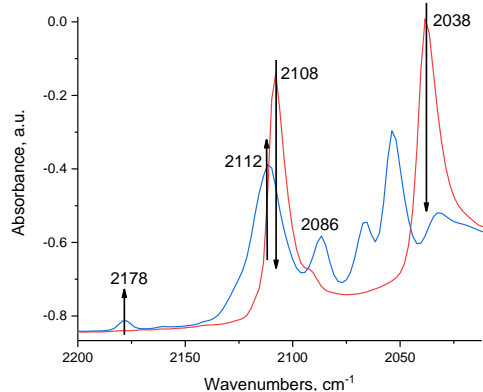


Figure 5. DRIFTS spectrum of 0.7% Ir(CO)₂/FAU Si/Al~15 during exposure to ethylene (~1 minute). 2,178 and 2,112 cm⁻¹ grow in concert.

The intense 2,112 cm⁻¹ band belongs to the CO vibration of an oxidized Ir center (CO adsorbed on metal cations has high molar extinction coefficients) and the low intensity 2,178 cm⁻¹ band corresponds to the Ir-H stretching vibration. Indeed, this fully agrees with the described synthesis of the first supported, transition metal carbonyl hydride complexes of Rh(III)(H)_x(CO)_{6-x} and relatively low intensity of Rh-H stretching vibrations compared to CO vibrations.^{17,18} We note that Rh(III) and Ir(III) have the same d⁶

electronic configuration and provide the analogous (to Rh) synthesis of Ir(III) carbonyl hydride complex¹⁸, unambiguously identifying the Ir-H stretch at 2,150 cm⁻¹. Analogous to the selective synthesis of Rh(III)(CO)H₂ complexes from Rh(CO)₂¹⁸, the Ir(CO)H_x species has been suggested from treatments of Ir(CO)₂/FAU with ethylene followed by hydrogen.³² In that study, the authors failed to identify the Ir-H stretch, concluding that its signature is too weak to be observed. We treated our Ir(CO)₂ materials with C₂D₄, forming first Ir(I)(CO)(C₂D₄) which we then exposed to H₂ flow (Figs. S29, S30, S31). Both the actual spectra and difference spectra indicate selective conversion of Ir(CO)(C₂D₄) to the Ir(CO)(H)₂ complex with CO stretching observed at 2,065 cm⁻¹ and the Ir-H stretch at 2,150 cm⁻¹. Isotopic shift experiments with D₂ (Fig. S31) confirm that the 2,150 cm⁻¹ is indeed the Ir-H stretch.

As such, the simultaneous formation of new Ir-H and Ir-CO stretches (Figs. 5 and 6) arises from the generation of one species. The high-lying stretch of Ir-CO means that Ir is in the +3 oxidation state, signifying the unprecedented oxidative addition of the C-H bonds of ethylene to the Ir(CO) fragment with the formation of Ir(III)(CO)(H)(C₂H₃) carbonyl vinyl hydrido-complex: C₂H₄-Ir(I)-CO ↔ C₂H₃-Ir(III)(H)(CO). These assignments and described behavior are further supported by observation of these species the the in situ NMR data (Figure S23).

As the concentration of this complex reaches its maximum (~1 minute), the intensities of both the 2,112 and 2,178 cm⁻¹ features reach their maxima and then decline in concert as a new CO stretching band develops at 2,086 cm⁻¹ that has no corresponding Ir-H stretching band (Figure 6). This indicates the hydride is consumed during the reaction with ethylene. This suggests the consequent formation of an Ir(III)(CO)(C₂H₅)(C₂H₃) complex via ethylene insertion into the Ir-H bond.

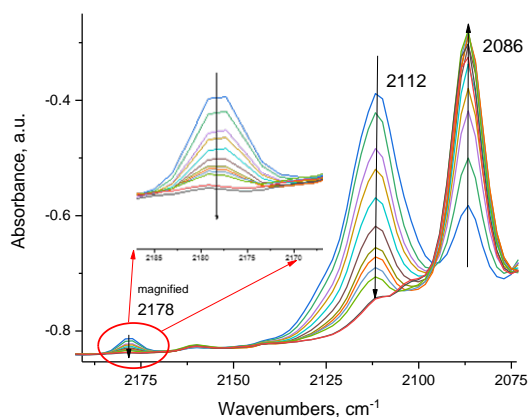


Figure 6. DRIFTS spectrum of 0.7% Ir(CO)₂/FAU during exposure to ethylene (~5 minutes). The 2,112 and 2,178 cm⁻¹ bands decline simultaneously as the 2,087 cm⁻¹ feature grows.

Furthermore, in order to unambiguously assign the 2,178 cm⁻¹ band to the Ir-H stretch, we replicated the infrared experiment on Ir(CO)₂ and C₂H₄ with C₂D₄. We observed the absence of the 2,178 cm⁻¹ band (Ir-H stretch), upon oxidative addition of C₂D₄ to the Ir(I) center. Instead, Ir(III)-D species forms (Fig. S32).

The observed room-temperature activation of C-H bonds with the formation of iridium carbonyl alkyl hydride complex is unprecedented. Such transformation have been only rarely described in organometallic literature⁴¹ and never directly observed spectro-

scopically on any solid material. The bond is not split heterolytically on the M-O bond but instead it is activated homolytically via oxidative addition to an electrophilic d^8 metal center in the zeolite micropore. High coordinative unsaturation and superelectrophilicity of M cations in zeolite have been recently quantified for isoelectronic d^8 Pd(II) ions,²² explaining why this reaction is favored over heterolytic activation of C-H bonds on covalent M-O bond. It is important to note that such a homolytic pathway of C-H bond activation has been previously overlooked in the metal/zeolite and M/oxide literature. Indeed, heterolytic activation of strong X-H bonds (C-H of hydrocarbons and N-H of ammonia) normally require relatively high temperatures.³³⁻³⁴

Ethylene activity over Ir(CO)₂/FAU produces measurable amounts of butenes at temperatures above 80°C and butadiene at temperatures above 180 °C with the maximum rate of catalytic butadiene production at ~200-220°C and selectivities to butadiene on the order 17-20% (Table S 2). After catalysis, Ir remains site-isolated and does not agglomerate into Ir nanoparticles as evidenced by HAADF-STEM and FTIR data (Figure 2D, S21,S22). Formation of carbonaceous polymeric deposits, framework breakage, and dealumination similar to Ni/BEA is also observed (Figs. S20, S21, S25). The ease with which oxidative addition of ethylene C-H bond to highly electrophilic Ir(I) center takes place at room temperature at 1 bar pressure of ethylene, suggests that C-H activation is not the rate-limiting step of the ethylene dimerization under these conditions: C-C coupling and/or beta-hydride elimination are expected to be rate-limiting steps in catalysis.

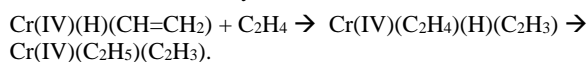
We construct two plausible catalytic pathways for butadiene (and butene) production. Two different steps of initial C-H bond activation are possible: 1) homolytic activation of C-H bond via oxidative addition to M d^8 center, which we observe experimentally (Figure S26) and 2) heterolytic activation of C-H bond on the M-Ozeolite pair (Figure S27), which we did not observe. Two ethylene molecules could also couple on single d^8 metal center with the formation of metallacyclopentane species (Figure S28), that were shown by Goldman and co-workers to form on Ir(C₂H₄)₂(Phebox) system by trapping via CO.³⁰ The stability of the species, as noted previously by Halpern,³⁵ does not mean that it is the true active state of the catalyst. Indeed, most active species are formed transiently (as we observe experimentally for Ir(III)(H)(CO)(C₂H₃) species), hence mechanism in Fig. S26 is most likely operative.

Furthermore, deeper mechanistic insight into the pathway of butadiene production was achieved by refuting the direct dehydrogenation of butene into butadiene. When butene-1 was introduced to the catalyst at 150-200°C, no butadiene was observed. Thus, the route to butadiene mechanistically differs from direct butene dehydrogenation. Indeed, such dehydrogenation does not take place on single Ir atoms under such mild conditions.

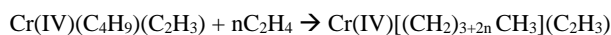
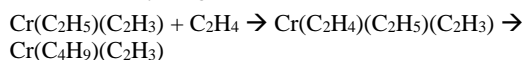
Notably, in the most probable reaction mechanism depicted in Fig. S26, we propose butene-1 formation directly from Ir(III)(CO)(C₂H₅)(C₂H₃) and Ni(IV)(C₂H₅)(C₂H₃) via reductive elimination of the ethyl and vinyl fragments with restoration of Ni(II) and Ir(I)-CO fragments which reform Ni(II)(C₂H₄) and Ir(I)(CO)(C₂H₄) in the presence of ethylene. It is also possible that beta-hydride elimination releases butane-1 from the M-(n-Butyl) intermediate, which forms when the ethyl group in M(C₂H₄)(C₂H₅) migrates. Butadiene may be formed analogous to this scheme but in this case the vinyl group of M(C₂H₃)(C₂H₄) fragment migrates, forming M-CH₂-CH₂-CH=CH₂, from which via beta-hydride elimination butadiene-1,3 is released.

These findings for supported Ni(II) and Ir(I) isolated sites may help reveal mechanistic uncertainties for the Cr/SiO₂ Phillips ethylene polymerization catalyst, extensively studied over 50 years. Though believed to follow a Cossee-Arlman Cr-alkyl mechanism, the low number of active sites (<10%), amorphous silica support, fast reaction rates, and the presence of multiple oxidation states of Cr prevented a thorough understanding of the initiation mechanism. Recent elegant studies³⁶ demonstrated that Cr(II) sites are required to start ethylene polymerization, and earlier kinetic studies suggested schemes consistent with activation of ethylene on Cr(II) sites to form Cr(IV) vinyl hydride³⁷⁻³⁸, though this species has never been observed. Based on our current findings, we suggest that the active fraction of the catalyst could be the highly electrophilic Cr(II) species that can add ethylene via C-H oxidative addition to form a Cr(IV)-vinyl (C₂H₃)-hydride (H) species: $Cr(II) + C_2H_4 \leftrightarrow Cr(IV)(H)(CH=CH_2)$

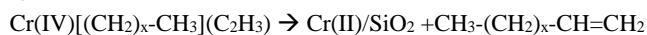
The formation of Cr-ethyl follows:



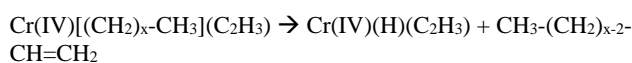
Cr(IV)(C₂H₅)(C₂H₃) sites may facilitate longer alkyl chain formation via alkyl migration:



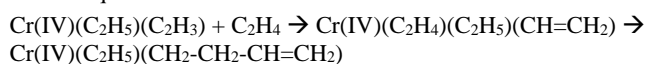
Subsequently, direct reductive elimination of CH₃(CH₂)_xCH=CH₂ is possible which restores the Cr(II) site and re-starts the catalytic cycle:



Beta-hydride elimination from Cr(IV)[(CH₂)_x-CH₃](C₂H₃) could also restore Cr(IV)(H)(C₂H₃) and re-start the polymerization cycle:



The proposed mechanism does not contradict experimental observations and provides a plausible explanation for the initiation uncertainties of the Phillips catalyst. Furthermore, support for this proposed mechanism is obtained from recent works, in which -CH₂-CH₂-CH=CH₂ sites were suggested to form on the catalyst.⁴² These sites can form from the vinyl migration in the following reaction sequence:



In conclusion, we provide the first experimental mechanistic evidence of how ethylene dimerization occurs and proceeds on d^8 M(I and II) cations in zeolites in the absence of an initial M-H species: the M-H bond is formed via the homolytic activation of ethylene's C-H bond (stronger than that of methane) on very electrophilic Ir(I) sites in the zeolite micropore. Further, the preparation of well-defined Ir(I) and Ni(II) d^8 in zeolites is demonstrated and accompanied by new chemistry and characterization for both systems before and after catalysis. Both Ni(II) and Ir(I) in zeolites produce butenes and, unprecedentedly, butadiene upon reaction with ethylene under mild conditions. Notably, Ni is more active at lower temperatures toward C-H bond activation than the expensive Ir.

ACKNOWLEDGMENTS

The research described in paper is part of the Quickstarter Initiative at Pacific Northwest National Laboratory. It was conducted

under the Laboratory Directed Research and Development Program at PNNL, a multiprogram national laboratory operated by Battelle for the U.S. Department of Energy. The research described in this paper was performed in the Environmental Molecular Sciences Laboratory (EMSL), a national scientific user facility sponsored by the DOE's Office of Biological and Environmental Research and located at the Pacific Northwest National Laboratory (PNNL). PNNL is operated for the US DOE by Battelle (DE-AC06-76RLO 1830, DE-AC05-RL01830, FW-47319).

Notes

The authors declare no competing financial interests.

REFERENCES

1. Sachtler, W. M. H., *Catal Today* **1992**, *15* (3-4), 419-429.
2. Klier, K., *Langmuir* **1988**, *4* (1), 13-25.
3. Lonyi, F.; Kovacs, A.; Szegedi, A.; Valyon, J., *J Phys Chem C* **2009**, *113* (24), 10527-10540.
4. Corma, A.; Garcia, H., *Topics in Catalysis* **2008**, *48* (1-4), 8-31.
5. Haruta, A., *Chemical Record* **2003**, *3* (2), 75-87.
6. Barrer, R., Surface Organometallic Chemistry: Molecular Approaches to Surface Catalysis. In *Zeolite Synthesis: An Overview*, Basset, J.-M.; Gates, B. C.; Candy, J.-P.; Choplin, A.; Leconte, M.; Quignard, F.; Santini, C., Eds. Kluwer Academic Publishers: 1988; pp 221-244.
7. Kwak, J. H.; Tran, D.; Burton, S. D.; Szanyi, J.; Lee, J. H.; Peden, C. H. F., *J Catal* **2012**, *289*, 272-272.
8. Sachtler, W. M. H., *Accounts of Chemical Research* **1993**, *26* (7), 383-387.
9. Khivantsev, K.; Jaegers, N. R.; Kovarik, L.; Hanson, J. C.; Tao, F.; Tang, Y.; Zhang, X. Y.; Koleva, I. Z.; Aleksandrov, H. A.; Vayssilov, G. N.; Wang, Y.; Gao, F.; Szanyi, J., *Angew Chem Int Edit* **2018**, *57* (51), 16672-16677.
10. Finiels, A.; Fajula, F.; Hulea, V., *Catal Sci Technol* **2014**, *4* (8), 2412-2426.
11. Baiale, J., US Patent: US3738977A 1971.
12. Khivantsev, K.; Vityuk, A.; Aleksandrov, H. A.; Vayssilov, G. N.; Blom, D.; Alexeev, O. S.; Amiridis, M. D., *Acs Catal* **2017**, *7* (9), 5965-5982.
13. Agirrezabal-Telleria, I.; Iglesia, E., *J Catal* **2017**, *352*, 505-514.
14. Yang, A. C.; Garland, C. W., *J Phys Chem-US* **1957**, *61* (11), 1504-1512.
15. Knozinger, H.; Thornton, E. W.; Wolf, M., *J Chem Soc Farad T 1* **1979**, *75*, 1888-1899.
16. Serna, P.; Gates, B. C., *Angew Chem Int Edit* **2011**, *50* (24), 5528-5531.
17. Khivantsev, K. PhD Thesis University of South Carolina, 2015.
18. Khivantsev, K.; Vityuk, A.; Aleksandrov, H. A.; Vayssilov, G. N.; Alexeev, O. S.; Amiridis, M. D., *J Phys Chem C* **2015**, *119* (30), 17166-17181.
19. Joshi, R.; Zhang, G. H.; Miller, J. T.; Gounder, R., *Acs Catal* **2018**, *8* (12), 11407-11422.
20. Brogaard, R. Y.; Olsbye, U., *Acs Catal* **2016**, *6* (2), 1205-1214.
21. Moussa, S.; Concepcion, P.; Arribas, M. A.; Martinez, A., *Acs Catal* **2018**, *8* (5), 3903-3912.
22. Khivantsev, K.; Jaegers, N. R.; Koleva, I. Z.; Aleksandrov, H. A.; Kovarik, L.; Engelhard, M.; Gao, F.; Wang, Y.; Vayssilov, G. N.; Szanyi, J., *Chemrxiv* **2019**.
23. Khivantsev, K.; Jaegers, N. R.; Kovarik, L.; Proding, S.; Derewinski, M. A.; Wang, Y.; Gao, F.; Szanyi, J., *Appl Catal a-Gen* **2019**, *569*, 141-148.
24. Khivantsev, K.; Gao, F.; Kovarik, L.; Wang, Y.; Szanyi, J., *J Phys Chem C* **2018**, *122* (20), 10820-10827.
25. Petkov, P. S.; Aleksandrov, H. A.; Valtchev, V.; Vayssilov, G. N., *Chemistry of Materials* **2012**, *24* (13), 2509-2518.
26. Pomalaza, G.; Capron, M.; Ordonsky, V.; Dumeignil, F., *Catalysts* **2016**, *6* (12).
27. Dagle, V. L.; Flake, M. D.; Lemmon, T. L.; Lopez, J. S.; Kovarik, L.; Dagle, R. A., *Appl Catal B-Environ* **2018**, *236*, 576-587.
28. Sushkevich, V. L.; Ivanova, I. I., *Appl Catal B-Environ* **2017**, *215*, 36-49.
29. Cohen, S. A.; Auburn, P. R.; Bercau, J. E., *Journal of the American Chemical Society* **1983**, *105* (5), 1136-1143.
30. Gao, Y.; Emge, T. J.; Krogh-Jespersen, K.; Goldman, A. S., *Journal of the American Chemical Society* **2018**, *140* (6), 2260-2264.
31. Jaegers, N. R.; Hu, M. Y.; Hoyt, D. W.; Wang, Y.; Hu, J. Z., Development and Application of In Situ High-Temperature, High-Pressure Magic Angle Spinning NMR. In *Modern Magnetic Resonance*, Webb, G. A., Ed. Springer International Publishing: Cham, 2017; pp 1-19.
32. Martinez-Macias, C.; Chen, M.; Dixon, D.; Gates, B. *Chem. Eur. J.* **2015**, *21*, 11825 – 11835.
33. Khivantsev, K.; Biancardi, A.; Fathizadeh, M.; Almalki, F.; Grant, J. L.; Tien, H. N.; Shakouri, A.; Blom, D. A.; Makris, T. M.; Regalbutto, J. R.; Caricato, M.; Yu, M., *Chemcatchem* **2018**, *10* (4), 736-742.
34. Hu, B.; Getsoian, A.; Schweitzer, N. M.; Das, U.; Kim, H.; Niklas, J.; Poluektov, O.; Curtiss, L. A.; Stair, P. C.; Miller, J. T.; Hock, A. S., *J Catal* **2015**, *322*, 24-37.
35. Goldman, A. S.; Landis, C. R.; Sen, A., *Angew Chem Int Edit* **2018**, *57* (17), 4460-4460.
36. Morra, E.; Martino, G. A.; Piovano, A.; Barzan, C.; Groppo, E.; Chiesa, M., *J Phys Chem C* **2018**, *122* (37), 21531-21536.
37. Kissin, Y. V.; Brandolini, A. J., *J Polym Sci Pol Chem* **2008**, *46* (16), 5330-5347.
38. Zielinski, P.; Lana, I. G. D., *J Catal* **1992**, *137* (2), 368-376.
39. Tsybulevski, A. M.; Kustov, L. M.; Weston, K. C.; Greish, A.A.; Tkachenko, O. P.; Kucherov, A. V. *Ind. Eng. Chem. Res.* **2012**, *51*, 7073–7080.
40. Szanyi, J. ; Paffett, M. T. *Microp. Mat.* **1996**, *7* , 201-218.

41. Haddleton, D. M.; Perutz, R. N. *J. Chem. Soc., Chem. Commun.* **1986**, 1734-1736.

42. Chakrabarti, A., Gierada, M., Handzlik, J. et al. *Top Catal* **2016**, 59, 725.

Supporting Information for

Catalytic activation of ethylene C-H bonds on uniform d⁸ Ir(I) and Ni(II) cations in zeolites: toward molecular level understanding of ethylene polymerization on heterogeneous catalysts

Nicholas R. Jaegers^{1,2,&,*}, Konstantin Khivantsev^{1,&,*}, Libor Kovarik¹, Daniel W. Klau¹, Jian Zhi Hu¹,
Yong Wang^{1,2} and Janos Szanyi^{1,&,*}

¹Institute for Integrated Catalysis, Pacific Northwest National Laboratory Richland, WA 99352 USA

²Voiland School of Chemical Engineering and Bioengineering, Washington State University, Pullman, WA 99163 USA

*corresponding authors: Nicholas.Jaegers@pnnl.gov, Konstantin.Khivantsev@pnnl.gov, Janos.Szanyi@pnnl.gov

Experimental Methods

Faujasite and Beta zeolites with Si/Al of ~15 and 12.5 respectively, were supplied by Zeolyst in the ammonium form. Transformation of faujasite to the H-form was conducted by calcination in flowing dry air at 400°C followed by evacuation at 10^{-5} Torr and 400°C. It was subsequently stored in a VAC moisture- and oxygen-free glovebox. Single iridium atoms were then anchored in the micropore supercages of the prepared H-FAU zeolite. To ensure suitable dispersion, a well-defined square planar $\text{Ir}(\text{CO})_2(\text{Acac})$ complex (strem, >98% purity) was delivered into the micropores via a non-polar solvent propagation method^{12,17,18}. More specifically, the precursor was dissolved in pentane (Sigma Aldrich, <10 ppm moisture) and introduced into the faujasite. Approximately 26 mg of the Ir complex was dissolved in ~10 ml dry pentane under intense stirring; then the solution was added through the needle into the Schlenk flask containing 2.00 grams of calcined dry H-FAU powder. $\text{Ir}(\text{CO})_2$ fragments anchors to the zeolite through framework oxygen adjacent to Al T-atoms during this process. The pentane solution was subsequently evacuated for 5 hours under 10^{-5} Torr vacuum, leaving a dry powder of 0.7 wt% Ir/H-FAU.

Ni-BEA was synthesized by the modified IWI method we previously reported. In this, the NH_4 -form of BEA with Si/Al~12.5 was used as the supporting zeolite. Nickel nitrate hexahydrate (Sigma Aldrich, 99.99%) was dissolved in a water/ammonia solution, producing a purple-coloured $[\text{Ni}(\text{II})(\text{NH}_3)_6]$ complex with concentration 0.0757 M. The ammonia concentration was ~1.5 M. One pore volume equivalent (~0.9 cc/g BEA) of this solution was slowly introduced into zeolite powder with carefully mixing each aliquot. The resulting paste was dried at 80 °C in flowing air and then calcined at 550°C for 5 hours in a box furnace, yielding 0.4 wt% Ni/H-BEA.

The in situ static transmission IR experiments for Ni/BEA were conducted in a home-built cell housed in the sample compartment of a Bruker Vertex 80 spectrometer, equipped with an MCT detector and operated at 4 cm^{-1} resolution. The powder sample was pressed onto a tungsten mesh which, in turn, was mounted onto a copper heating assembly attached to a ceramic feedthrough. The sample could be resistively heated with temperature monitoring by a thermocouple spot welded onto the top center of the tungsten grid. Cold fingers on the CO-containing glass bulb were cooled with liquid nitrogen to prevent contamination by metal carbonyls. NO was cleaned with multiple freeze-pump-thaw cycles. Special-grade ethylene (OxArc) with 99.995% purity was cleaned with liquid nitrogen prior to use to remove traces of moisture. The activated sample was employed as the spectrum background. Each spectrum reported is obtained from the average of 256 scans. Experiments at 77 K were performed with liquid nitrogen used as a coolant. Prior to FTIR measurements, the sample was activated by heating under vacuum at 200°C to remove moisture. All dosed gases were undiluted.

DRIFTS spectra for Ir/FAU were recorded on a Nicolet iS50R FTIR spectrometer at 4 cm^{-1} resolution. The Ir/FAU powder was packed into the DRIFTS cell inside the dry glovebox, sealed and transferred to the FTIR where it was immediately connected to the gas manifold and exposed to flowing dry He. Special-grade ethylene (99.995% purity, OxArc) and UHP C_2D_4 was used for all experiments and UHP He flowing through oxygen and moisture traps was used as the inert gas. Spectra were referenced to an H-FAU background and 64 scans were averaged in each spectrum. Samples were loaded in a dry N_2 glovebox and transferred under N_2 to the infrared spectrometer. First the sample was purged with helium, and then experiments with pure ethylene or hydrogen flow were performed. Flow rates were ~10 cc/min.

HAADF-STEM analysis was performed with an FEI Titan 80-300 microscope operated at 300 kV. The instrument is equipped with a CEOS GmbH double-hexapole aberration corrector for the probe-

forming lens which allows for imaging with 0.1 nm resolution in scanning transmission electron microscopy mode (STEM). The images were acquired with a high angle annular dark field (HAADF) detector with inner collection angle set to 52 mrad. The fresh Ir/FAU sample was loaded with no exposure to air. Spent Ir/FAU (220°C under typical reaction conditions) was cooled down in the plug-flow reactor, purged with inert gas, and stored in the glove box prior to loading into HAADF-STEM without exposure to air. The images were collected in various projection, tilted slightly off the zone axis (to better visualize the Ir atoms), and imaged immediately to minimize beam damage during the experiment. EDS maps of O, Si, Al, and Ni were obtained for Ni/BEA in order to better visualize presence of low-contrast Ni (compared to high-contrast Ir).

The reaction measurements were performed in a typical plug-flow quartz reactor. Samples were loaded into the reactor in the glove box and purged with dry (Restek O₂/H₂O traps) He before reaction. Ethylene (OxArc, 99.995% purity) was delivered into the system through a separate set of moisture and oxygen traps. Approximately ~30 mg of catalyst powder was loaded into the quartz reactor for each run. The ethylene flow rate was ~10 sccm/min in the undiluted stream to achieve a residence time of ~0.2 s. An Agilent 7890 Gas Chromatograph equipped with an FID was used to analyze the system effluent. An Agilent HP-PLOT/Q column (30m, 0.53, 40µm film) was used for separation. Hydrocarbons response factors were calibrated with hydrocarbon mixtures.

²⁷Al MAS NMR measurements were performed at room temperature on a Bruker 850 MHz NMR spectrometer operating at a magnetic field of 19.975 T. The corresponding ²⁷Al Larmor frequency was 221.413 MHz. All spectra were acquired at a sample spinning rate of 18.0 kHz (± 5 Hz) and externally referenced to 1.0 M aqueous Al(NO₃)₃ (0 ppm). ¹³C and ¹H-¹³C CP measurements were conducted on a Varian Inova 300 MHz spectrometers. The corresponding ¹³C Larmor frequency was 75.43 MHz. Spectra were externally referenced to adamantane at 38.48 ppm and a sample spinning rate of 3.4 kHz at the magic angle was employed.

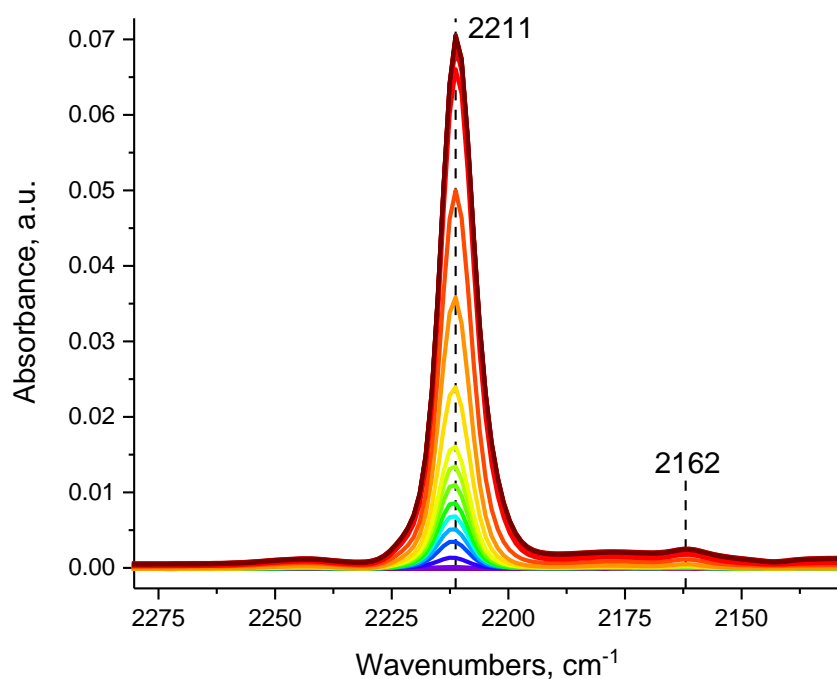


Figure S1. FTIR during CO adsorption on dry 0.4% Ni/BEA, $P(\text{CO})_{\text{max}} = 5 \text{ Torr}$.

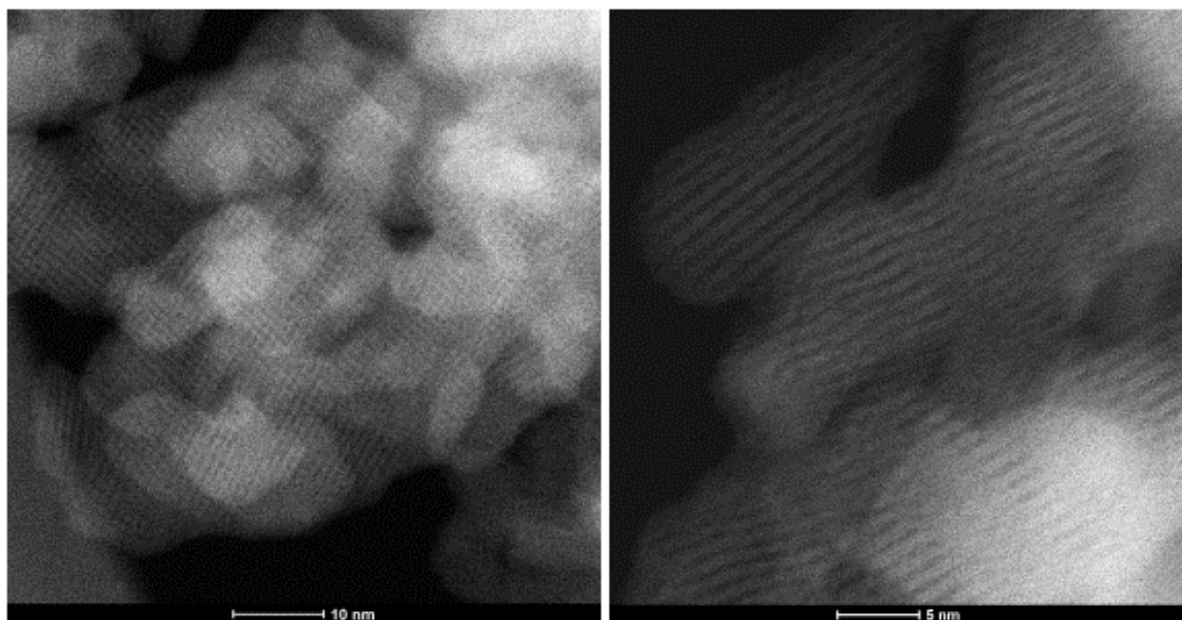


Figure S2. HAADF-STEM images of 0.4% Ni/BEA in different projections.

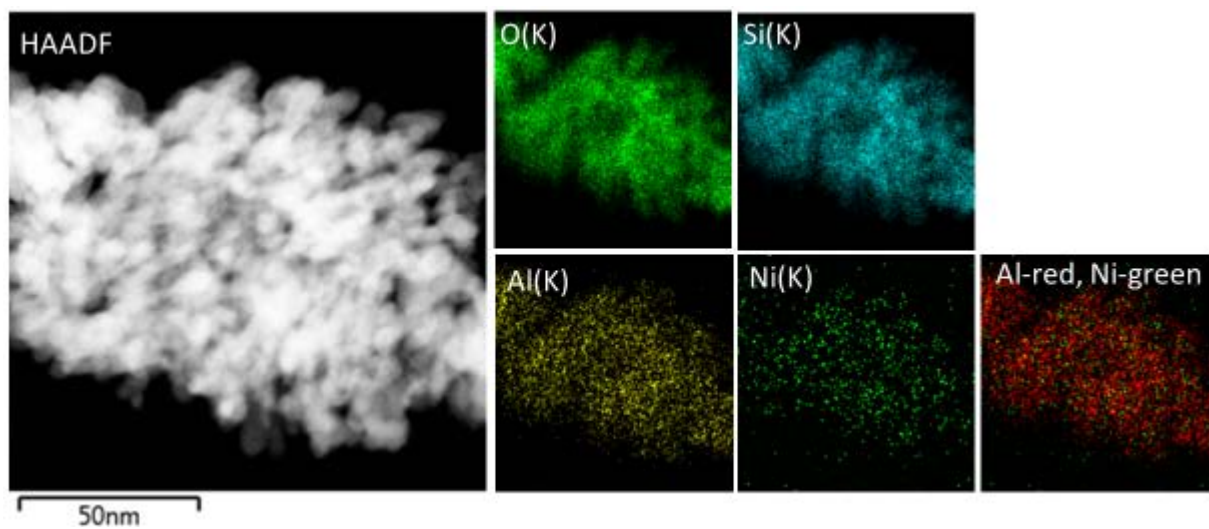


Figure S3. EDS maps of 0.4% Ni/BEA for O, Si, Al, Ni, overlay of Al and Ni maps, as well as the corresponding HAADF-STEM image for which EDS maps were collected.

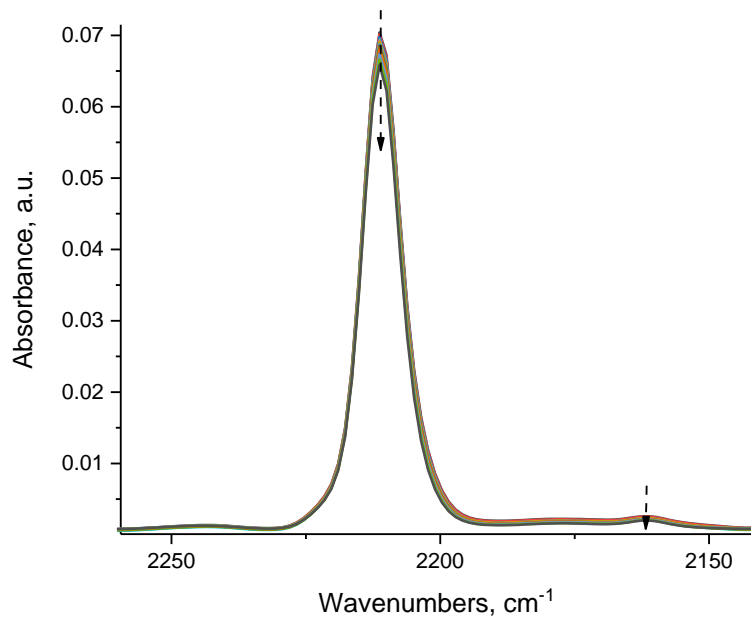


Figure S4. FTIR during vacuuming of Ni(II)-CO complex; Ni(II)-CO resists evacuation at RT. Final $P=0.05$ Torr.

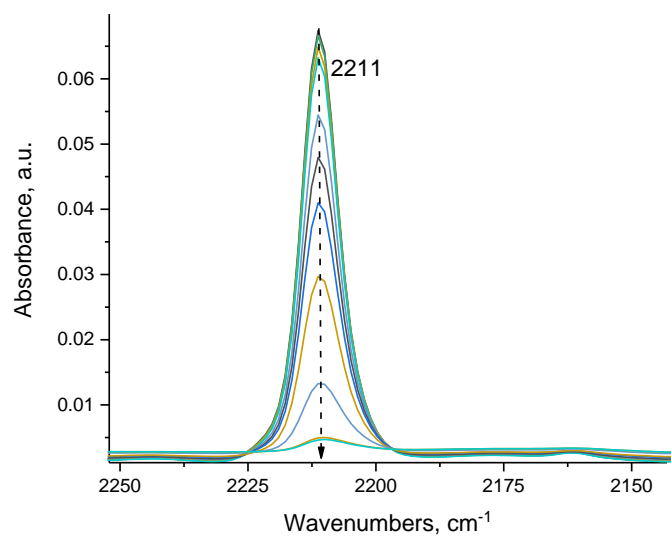


Figure S5. FTIR during ethylene adsorption (5 Torr) on Ni(II)-CO complex at RT. Ethylene completely displaces CO $\text{Ni(II)-CO} + \text{C}_2\text{H}_4 \rightarrow \text{Ni-(C}_2\text{H}_4) + \text{CO}$

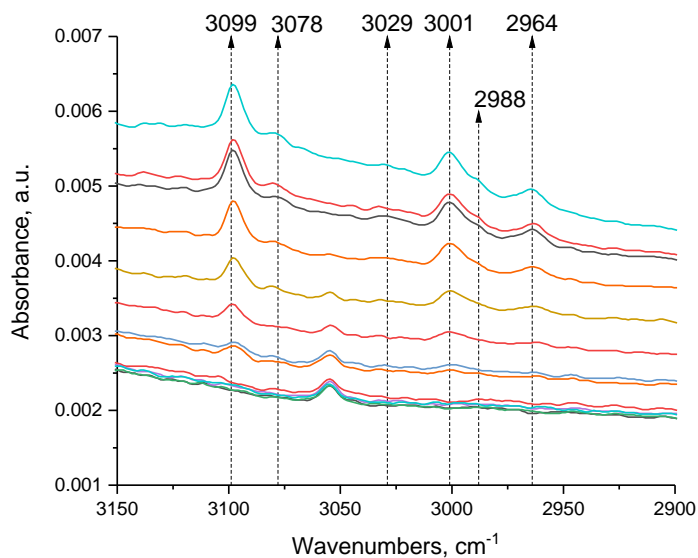


Figure S6. FTIR in the CH-stretching region during ethylene adsorption (5 Torr) on Ni(II)-CO complex at RT. The bands at 3,099, 3,078, 3,029 and 3,001 cm^{-1} are typical for π -coordinated $\text{H}_2\text{C}=\text{CH}_2$ adsorbed on a d^8 metal center in organometallic compounds, such as in Rh(I) and Pd(II) in zeolite (ref 22 in the main text).

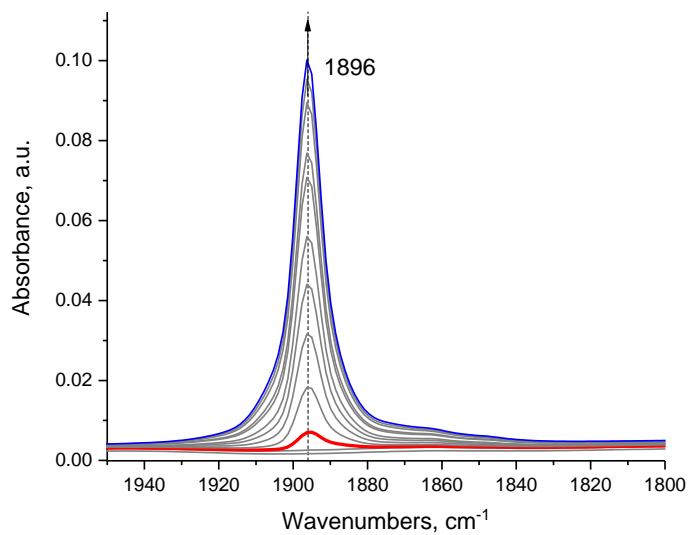


Figure S7. FTIR during NO adsorption on dry 0.4% Ni/BEA, $P(\text{NO})_{\text{max}}=5$ Torr; One type of Ni(II)-NO complex is formed. The FWHM of the NO band is $\sim 12 \text{ cm}^{-1}$.

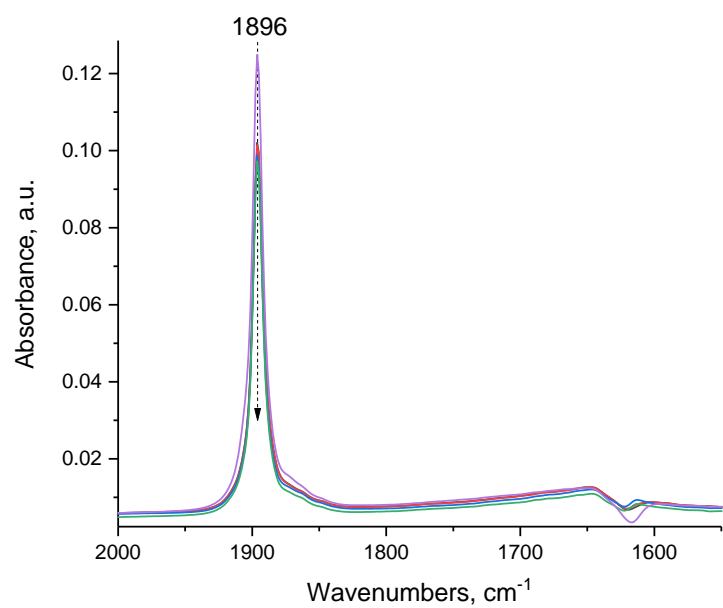


Figure S8. FTIR during vacuuming of Ni(II)-NO complex; Ni(II)-NO resists evacuation at RT. Final P=0.02 Torr.

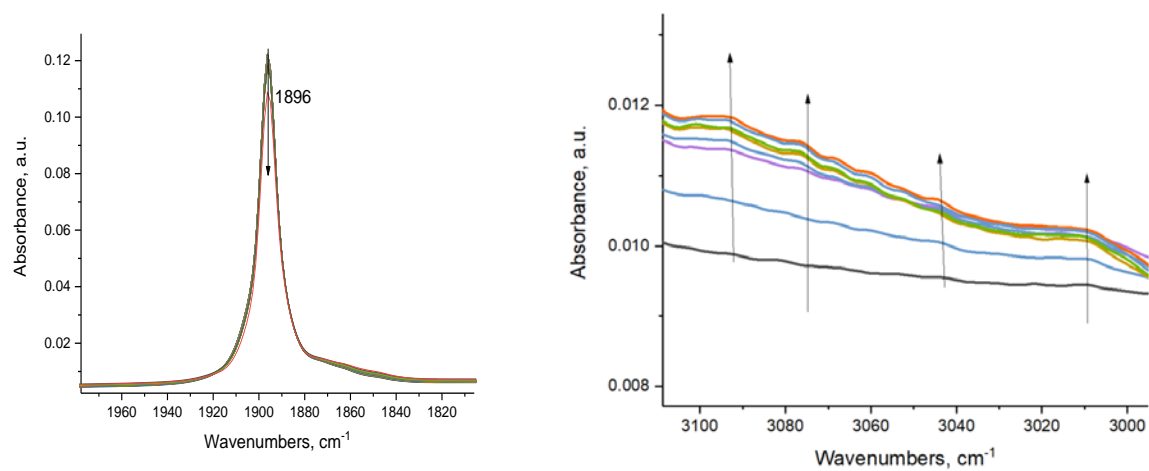


Figure S9. FTIR during ethylene adsorption (0.2 Torr) at RT on Ni(II)-NO. Ethylene displaces NO: $\text{Ni(II)-NO} + \text{C}_2\text{H}_4 \rightarrow \text{Ni-(C}_2\text{H}_4) + \text{NO}$

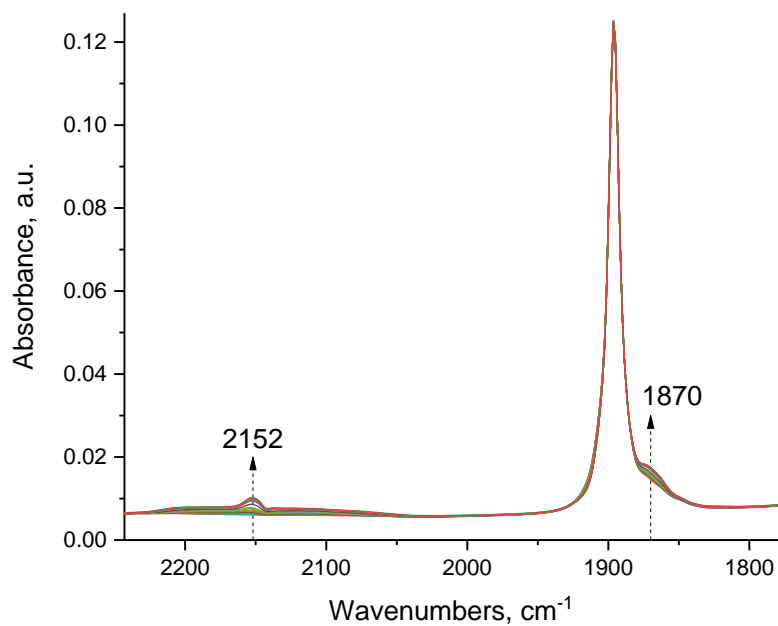


Figure S10. FTIR during CO adsorption (1 Torr) on the Ni(II)-NO complex. Ni(II)-NO is not displaced by CO, instead it forms Ni(II)(NO)(CO) complex with CO stretch at 2,152 cm^{-1} and NO stretch at 1,870 cm^{-1} .

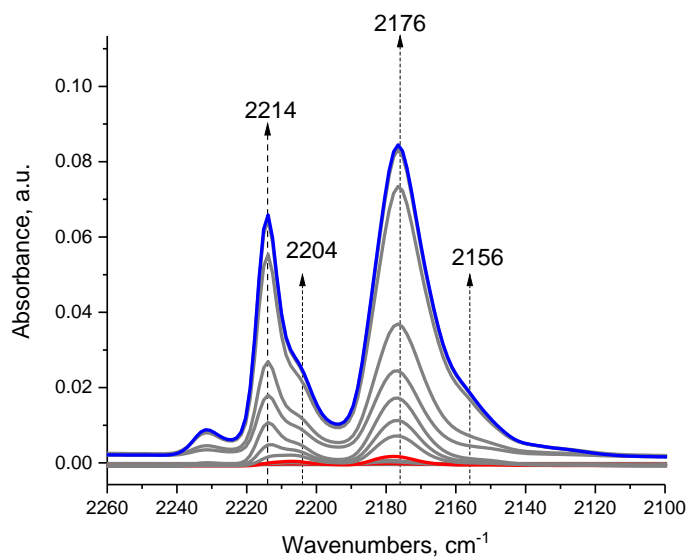


Figure S11. FTIR during CO adsorption (5 Torr) on 0.4% Ni(II)/BEA at liquid nitrogen (77 K) temperature. 2,214 and 2,204 cm^{-1} belong to CO adsorbed on Ni(II) ions. The 2,176 cm^{-1} band belongs to CO adsorbed on Brönsted acid protons of H-BEA, the 2,156 cm^{-1} band is CO interacting with silanols.

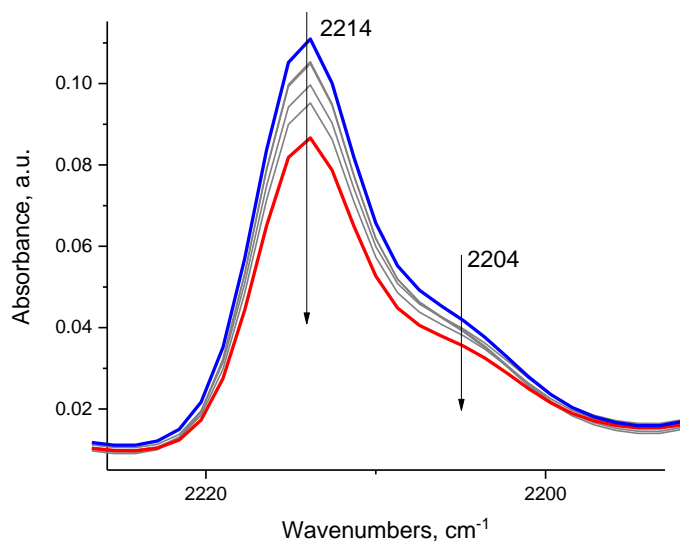


Figure S12. FTIR during vacuuming at liquid nitrogen temperature (77 K) of Ni(II)-CO complexes.

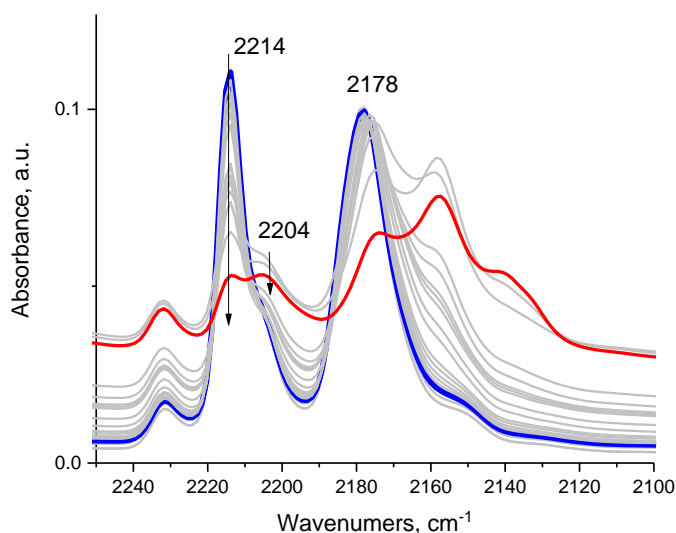


Figure S13. FTIR during C_2H_4 adsorption (2 Torr) at liquid nitrogen temperature (77 K) on Ni(II)-CO complexes. The 2,214 and 2,204 cm^{-1} CO bands of Ni(II)-CO complexes demonstrate markedly different behavior: the 2,214 cm^{-1} band decreases quickly but the 2,204 cm^{-1} band is relatively stable. This indicates that 2,214 and 2,204 cm^{-1} bands do not belong to a Ni(II)(CO)₂ dicarbonyl complex but to two different Ni(II)-CO complexes, in which the 2,214 cm^{-1} [belonging to one Ni(II)-CO complex] is very susceptible to ligand replacement with ethylene even at 77K: $Ni(II)-CO + C_2H_4 \rightarrow Ni(II)-C_2H_4 + CO$. Peculiarly, C_2H_4 easily displaces CO adsorbed on Brønsted acid protons of H-BEA (band at 2176 cm^{-1}).

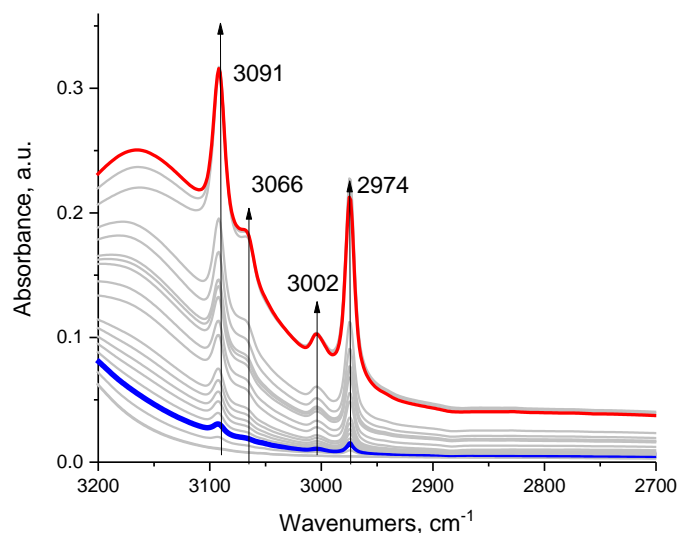


Figure S14. FTIR in the CH-stretching region during C_2H_4 adsorption (2 Torr) at liquid nitrogen temperature (77 K) on Ni(II)-CO complexes that were formed at 77 K (complimentary to Figure S13). The unusually intense bands at 3,091-2,074 cm^{-1} correspond to pi-coordinated $H_2C=CH_2$ interacting with $-OH$ groups of zeolite: although this interaction is much weaker at RT, at liquid nitrogen such complexes are significantly more stable, thus the high intensity of these bands.

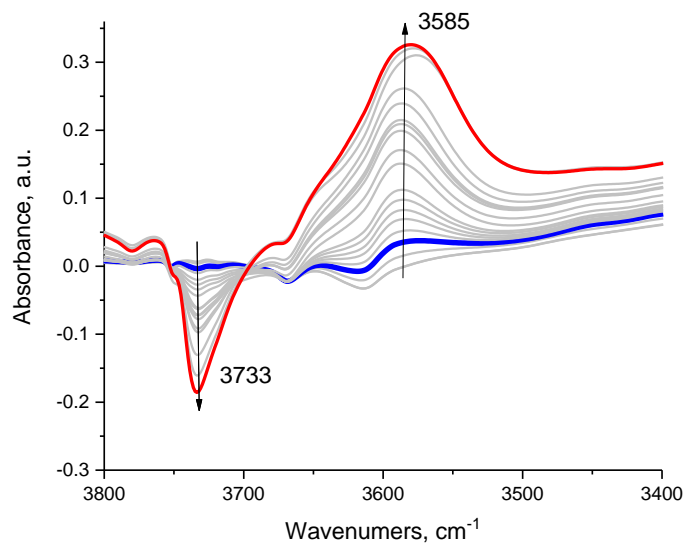


Figure S15. FTIR in the OH-stretching region during C_2H_4 adsorption (2 Torr) at liquid nitrogen temperature (77 K) on Ni(II)-CO complexes that were formed at 77 K (complimentary to Figure S13). OH bands of silanols at $\sim 3,730$ cm^{-1} decreases and forms a broad band at $\sim 3,580$ cm^{-1} due to formation of $-OH$ -Ethylene adducts.

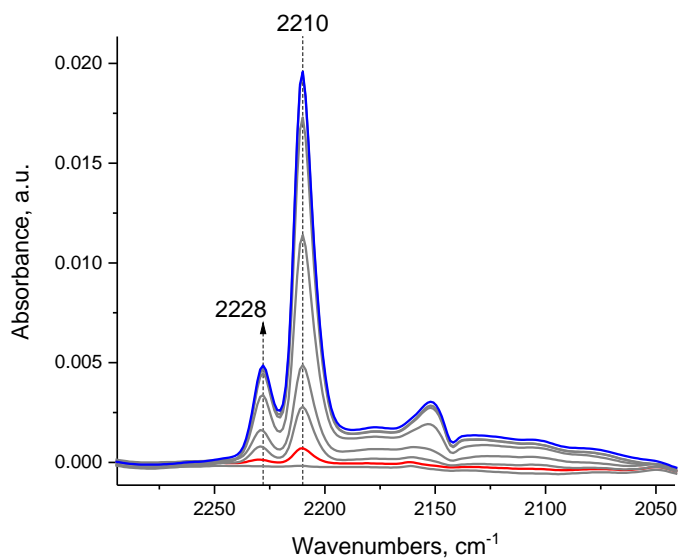


Figure S16. FTIR during CO adsorption (5 Torr) at RT on 0.4% Ni/BEA after C₂H₄ catalysis for 1 hr at 200°C in the FTIR cell.

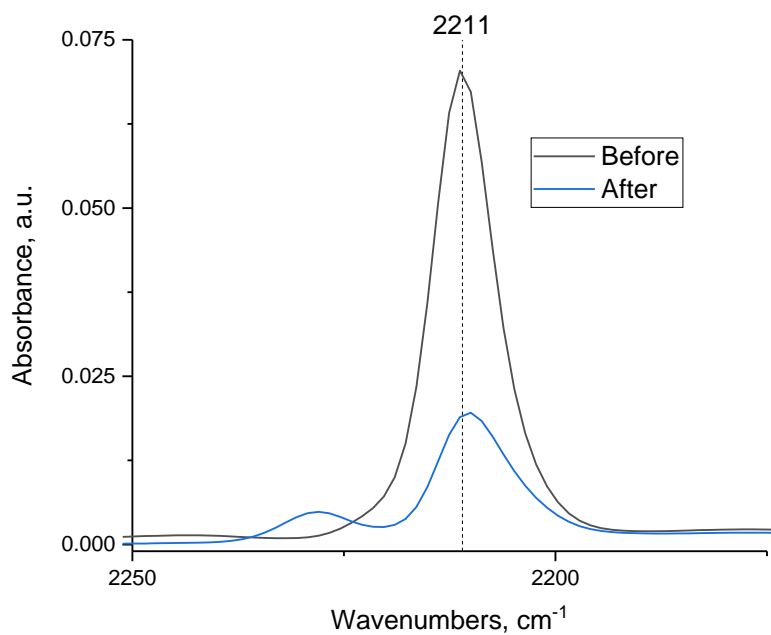


Figure S17. FTIR during adsorption of CO on dry 0.4% Ni/BEA $P(\text{CO})_{\text{max}}=5$ Torr, before and after exposed to C₂H₄ at 200°C in the FTIR cell for 1 hr; Only one type of Ni(II)-CO complex forms. The $\sim 2,228$ cm⁻¹ CO band is ascribed to CO adsorbed on extra-framework Al(III) sites. The FWHM of the CO band is ~ 9 -10 cm⁻¹.

Table S1. Initial TOF (with respect to butadiene formation) and selectivity to butadiene for 0.4% Ni/BEA. Conditions: 30 mg, C₂H₄ flow rate 10 sccm/min, GHSV ~ 40,000 hr⁻¹

Temperature, °C	Initial TOF, hr ⁻¹	Initial Selectivity, %
80	6.7	35
120	122	65
200	203	29
250	180	31

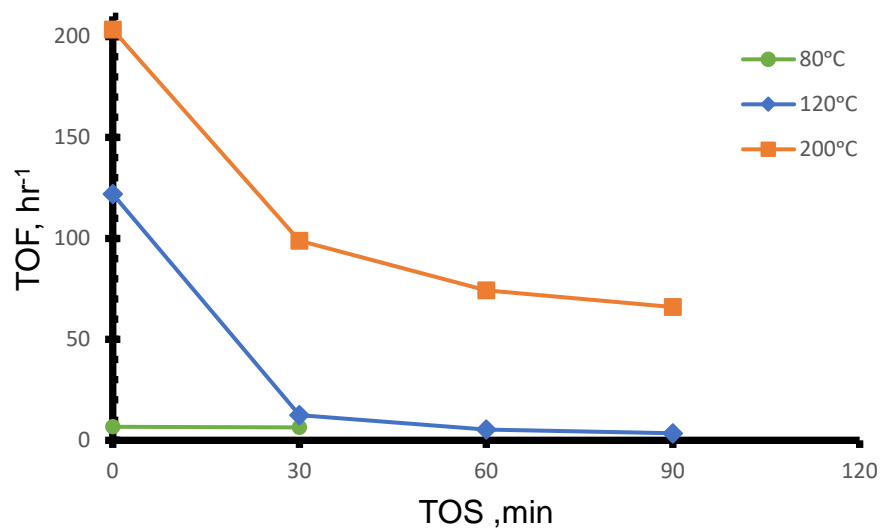


Figure S18. TOF (with respect to butadiene formation) trends as a function of time on stream for 0.4% Ni/BEA. Conditions: 30 mg, C₂H₄ flow rate 10 sccm/min, GHSV ~ 40,000 hr⁻¹

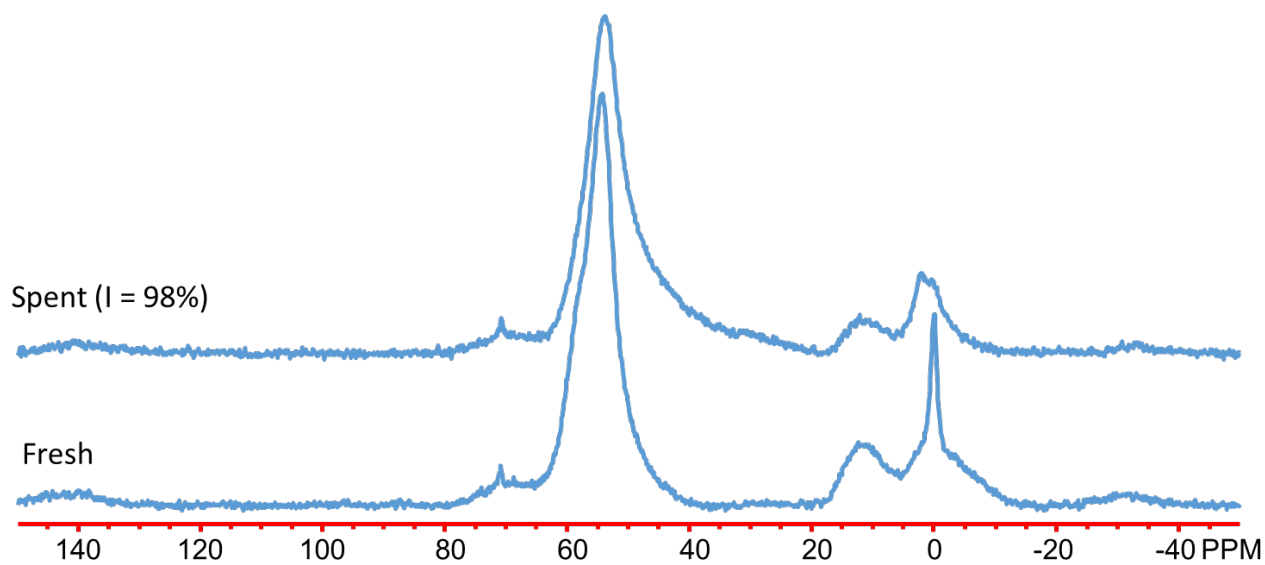


Figure S19. ²⁷Al MAS Solid-state NMR spectra for 0.4% Ni/BEA fresh (before catalysis) and spent (after C₂H₄ catalytic reaction at 220°C for 1 hour).

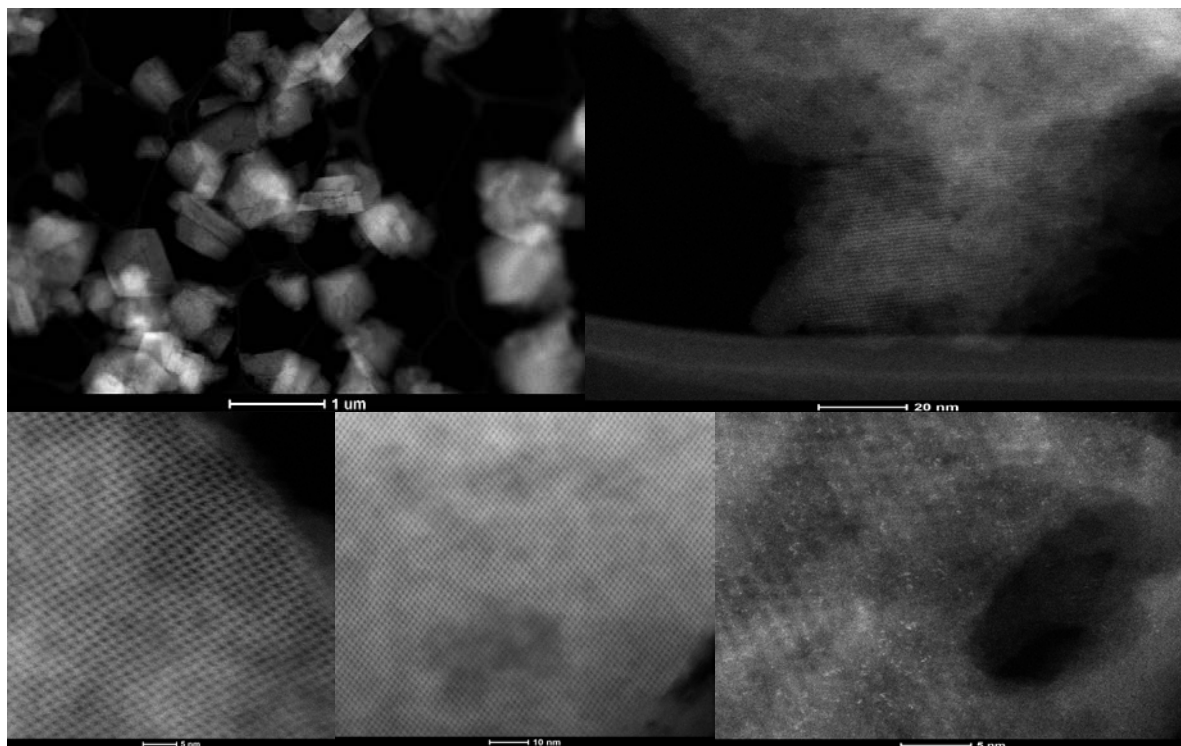


Figure S20. Additional HAADF-STEM images of 0.7% Ir(CO)₂/FAU in low magnification (showing absence of Ir nanoparticles) and high-magnification (showing presence of well-dispersed Ir atoms).

Table S 2. Initial TOF (with respect to butadiene formation) and selectivity to butadiene for 0.7% Ir(CO)₂/FAU Conditions: 30 mg, C₂H₄ flow rate 10 sccm/min, GHSV ~ 40,000 hr⁻¹

Temperature, °C	Initial TOF, hr ⁻¹	Initial Selectivity, %
80	0	0 (100% selective to butenes, TOF ~1.5)hr
180	0	0 (100% selective to butenes, TOF ~ 20)hr
225	203	29
250	180	31

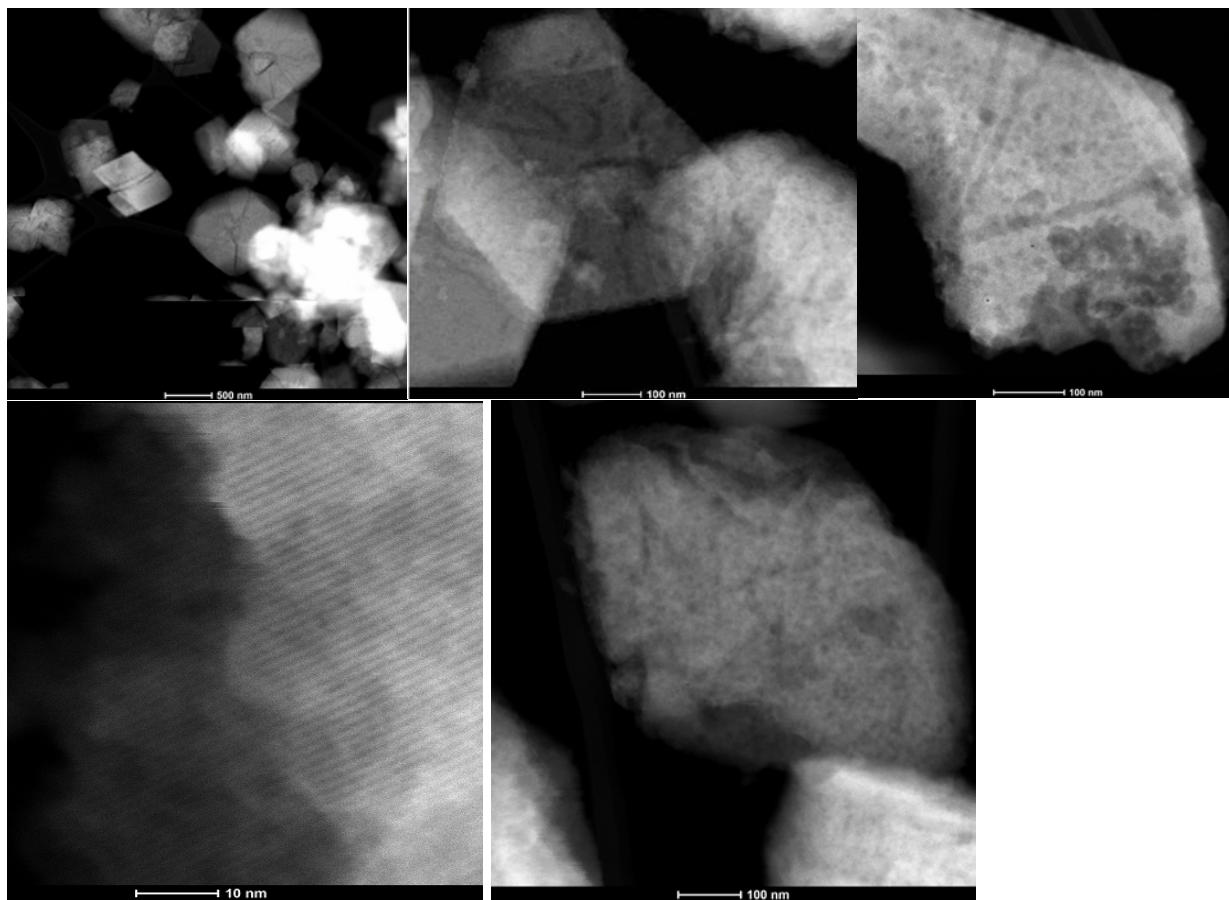


Figure S21. Additional HAADF-STEM images of 0.7% Ir(CO)₂/FAU, in low magnification and high-magnification after C₂H₄ catalysis at 200°C. The sample was transferred from the reactor into the HAADF-STEM in a special sample holder void of oxygen and moisture.

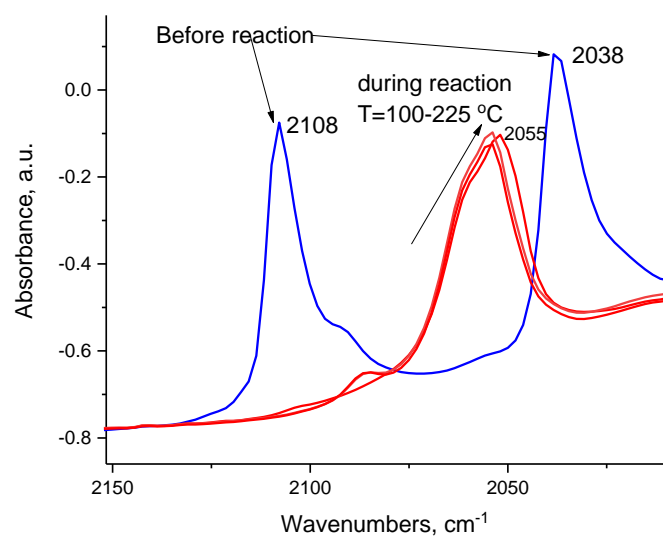


Figure S22. DRIFTS during Ir(CO)₂ reaction under pure C₂H₄ flow at 80-220°C. Ir(CO)(C₂H₄) is the only stable complex observed under these conditions.

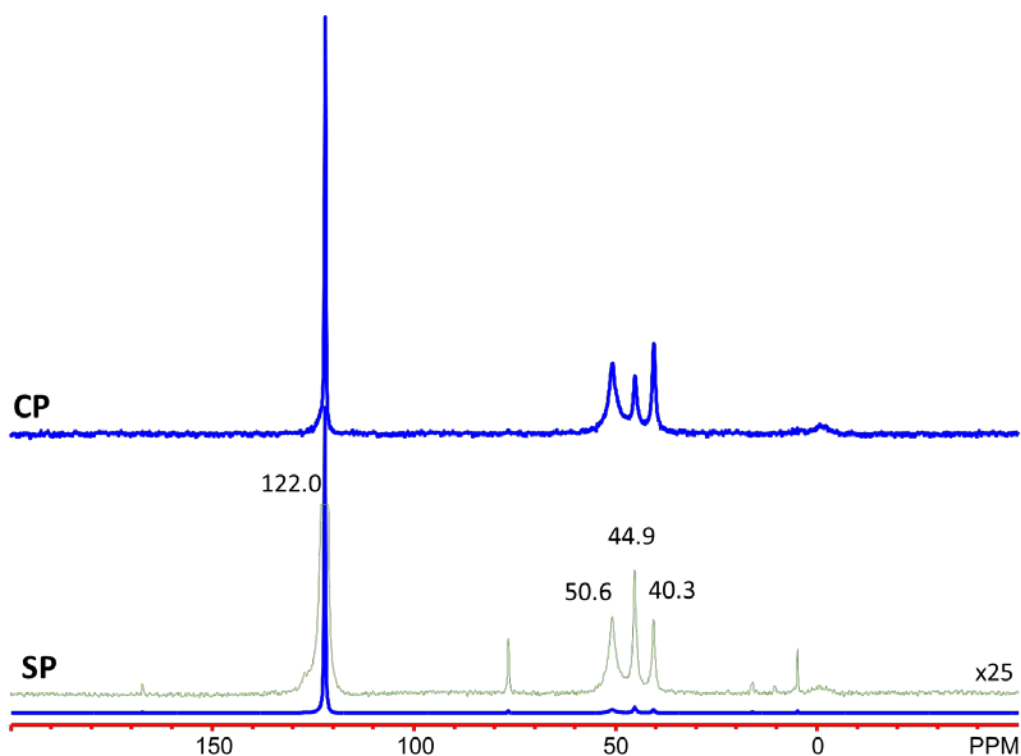


Figure S23. ^{13}C and $^1\text{H}\text{-}^{13}\text{C}$ CP MAS NMR spectra of 0.7% $\text{Ir}(\text{CO})_2/\text{FAU}$ after exposure of $-2'' \text{Hg } ^{13}\text{C}_2\text{H}_4$ at room temperature. The MAS speed was 3,418 Hz. Peaks are assigned to ethylene (122 ppm, SSB: 167, 76.3 ppm), π -coordinated ethylene ligands (50.6 ppm, [J. Phys. Chem. B 2005, 109, 51, 24236-24243]), and vinyl [Bulletin of the Academy of Sciences of the USSR, Division of chemical science, 1981, Volume 30, Issue 8, pp 1581, ^{13}C NMR spectra and structure of iron carbonyl π complexes of vinylsilanes] (44.9 and 40.3 ppm), further supporting the infrared spectroscopy results. CP refers to cross-polarization. SP referese to single pulse.

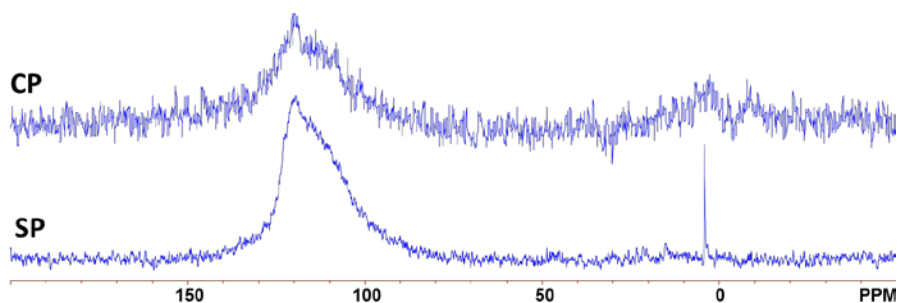


Figure S24. ^{13}C MAS Solid-state NMR spectra for 0.7% $\text{Ir}(\text{CO})_2/\text{H-FAU}$ after in situ reaction with $^{13}\text{C}_2\text{H}_4$ at 150°C for 1 hr. Polymeric carbonaceous deposits are observed as a broad band in Cross-Polarization spectra between 80 and 150 ppm. Gas phase ethane is also present (4 ppm). [App. Cat. 1988, 45, 345-356] CP refers to cross-polarization. SP referese to single pulse.

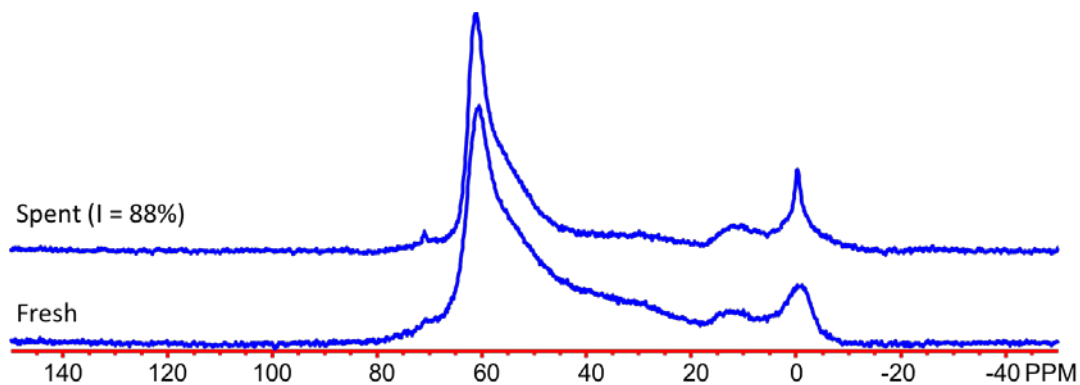


Figure S25. ^{27}Al MAS Solid-state NMR spectra for 0.7% $\text{Ir}(\text{CO})_2/\text{FAU}$ with Si/Al-15 fresh (before catalysis) and spent (after C_2H_4 catalytic reaction at 225°C for 1 hour).

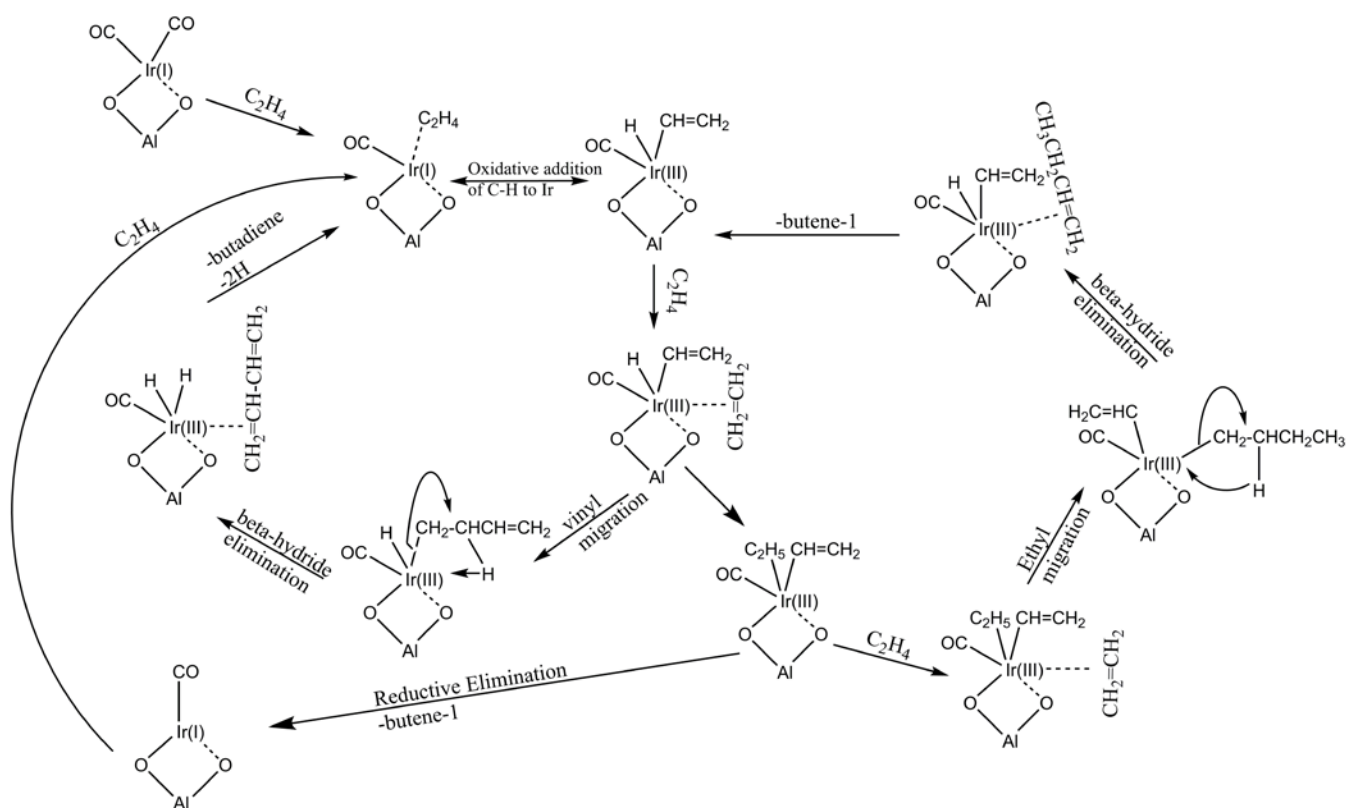


Figure S26. Probable mechanism for butene and butadiene formation from ethylene on $\text{Ir}(\text{CO})_2/\text{FAU}$ and Ni/BEA . In this mechanism C-H bond of ethylene is activated homolytically. Note, that completely analogous steps apply for $\text{Ni}(\text{II})/\text{BEA}$ system, except in that case no CO molecule is adsorbed on Ni. Oxidative addition of C-H bond of ethylene to $\text{Ni}(\text{II})$ produces $\text{Ni}(\text{IV})(\text{H})(\text{C}_2\text{H}_3)$ nickel (IV) vinyl hydride species. Coordination of the metal atom to the zeolite framework is shown only as a representation and could be flexible.

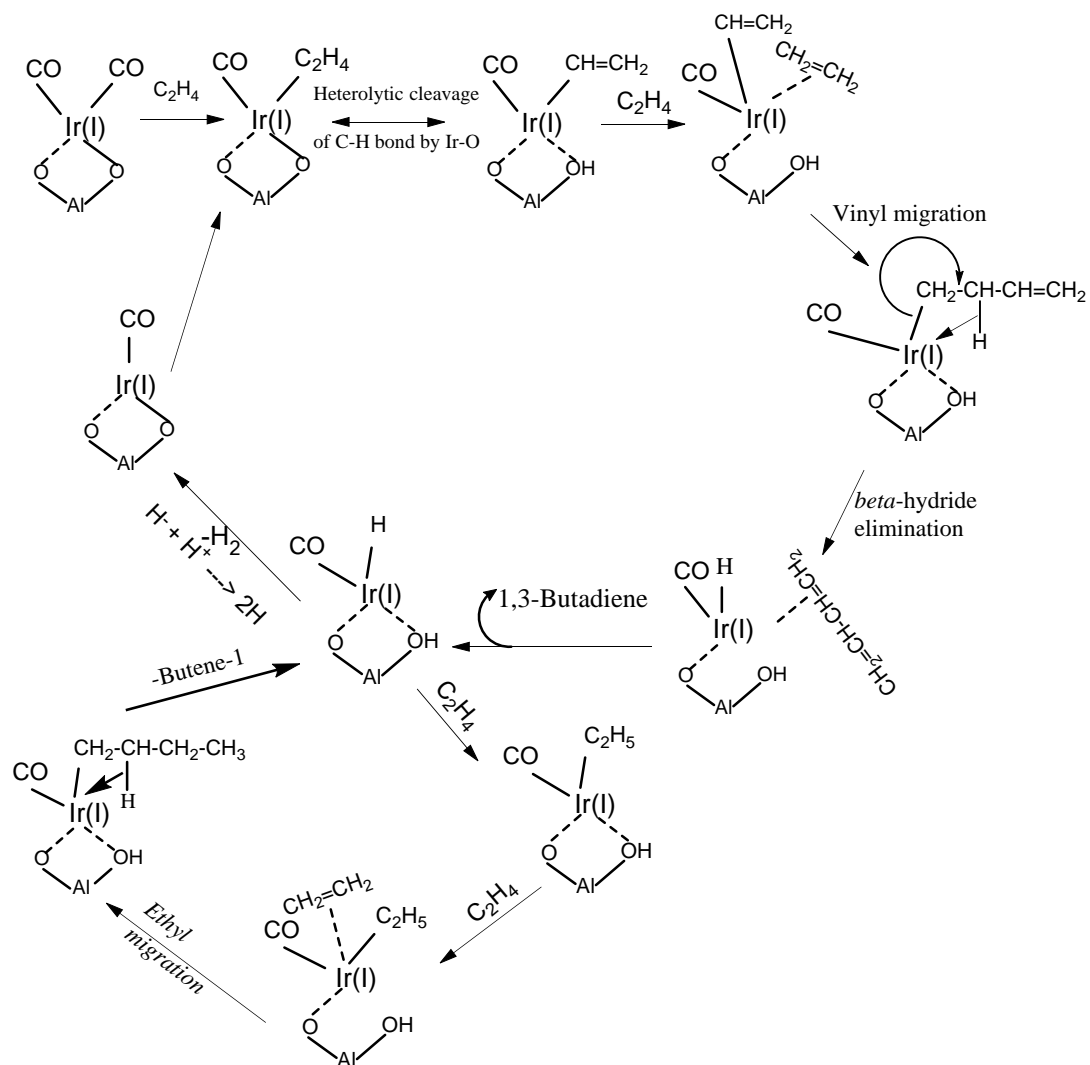


Figure S27. Probable mechanism for butene and butadiene formation from ethylene on $Ir(CO)_2/FAU$ and Ni/BEA . In this mechanism, C-H bond of ethylene is activated heterolytically on Ir(I)-O and Ni(II)-O bonds. Note, that completely analogous steps apply for Ni(II)/BEA system, except in that case no CO molecule is adsorbed on Ni. Coordination of the metal atom to the zeolite framework is shown only as a representation and could be flexible.

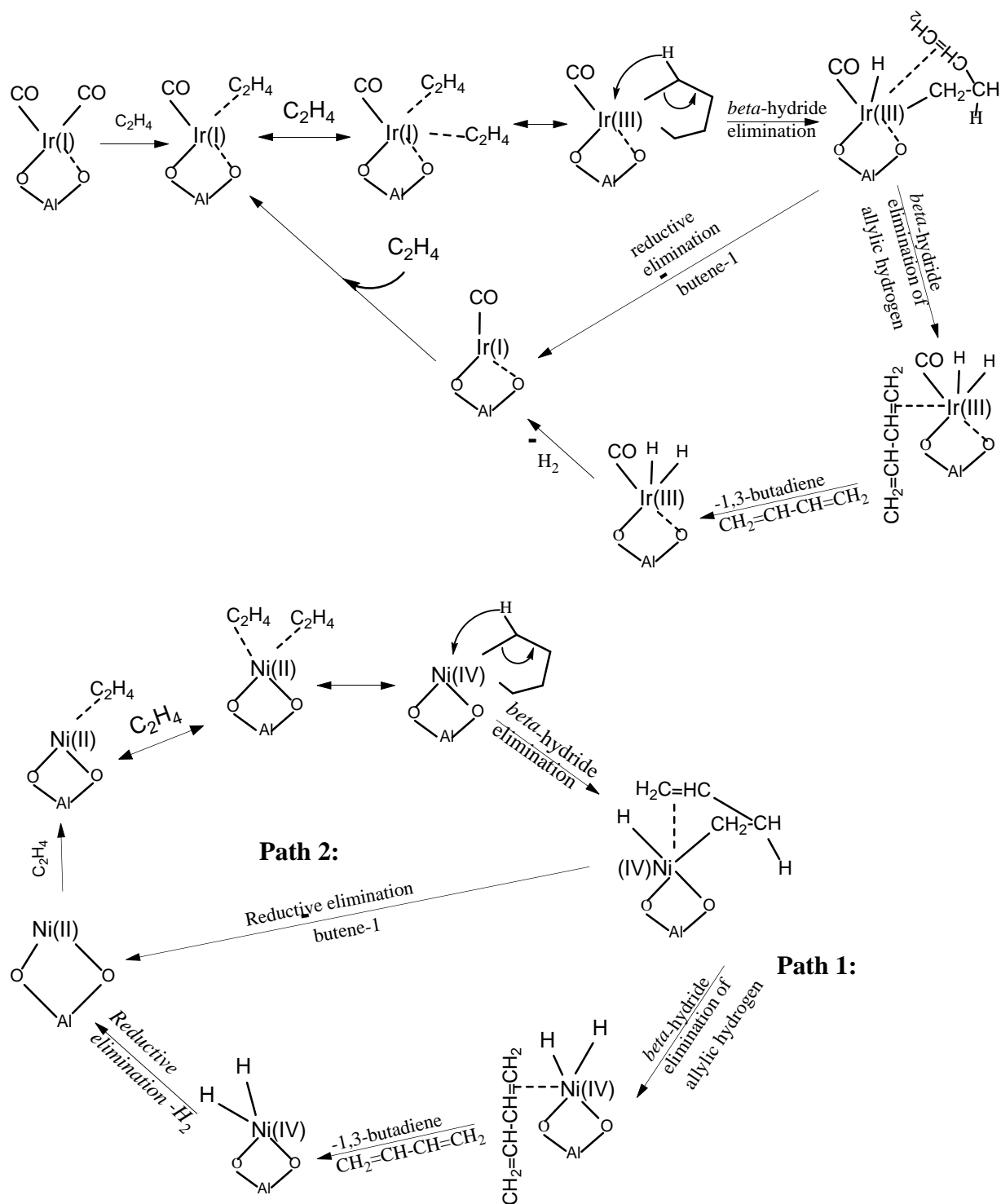


Figure S28. Mechanism for butene and butadiene formation from ethylene on $Ir(CO)_2/H$ -FAU and Ni/BEA viametallocyclopentane intermediates. In this mechanism, two ethylene molecules couple on Ir(I) and Ni(II) sites with the formation of Ir(III) iridacyclopentane and Ni(IV) nickelacyclopentane intermediates initially. In the case of Ni, no CO molecules are coordinated to Ni(II). Coordination of the metal atom to the zeolite framework is shown only as a representation and could be flexible.

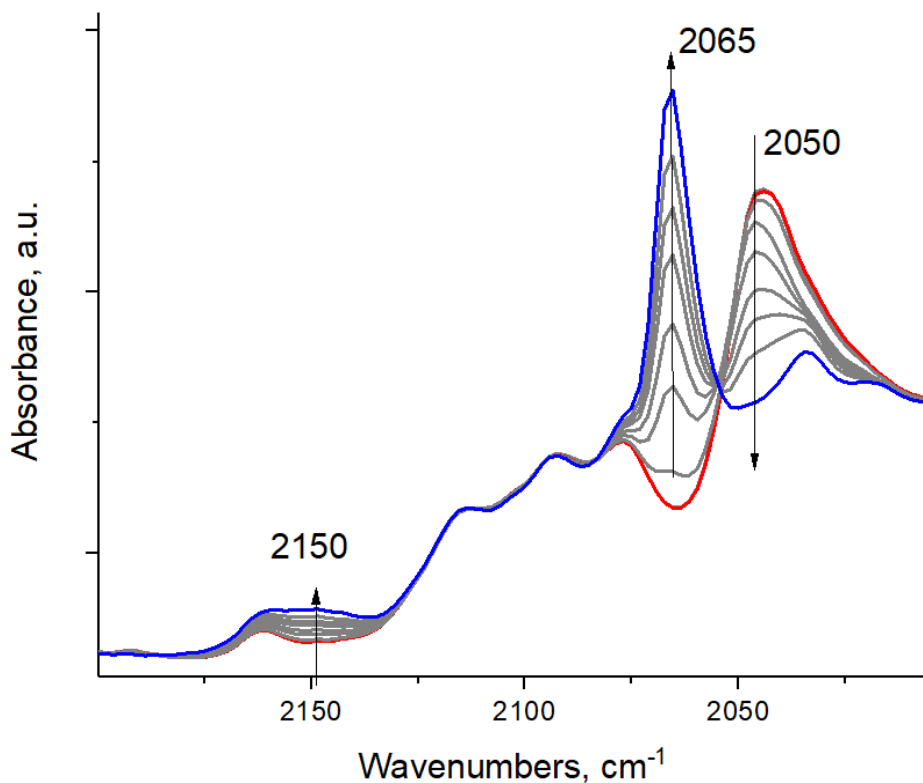


Figure S29. DRIFTS over time (1-5 minutes) of Ir(CO)(C₂D₄) during reaction with pure H₂ (H₂ flow ~10 cc/min). CO band of Ir(CO)(C₂D₄) at ~2,050 cm⁻¹ selectively goes down and a new CO band grows at 2,065 cm⁻¹. Simultaneously, a weak band develops at 2,150 cm⁻¹, assigned to Ir-H stretch. The selective formation of Ir(III)(CO)H₂ complex takes place: Ir(I)(CO)(C₂H₄) + 2 H₂ → Ir(III)(CO)(H)₂ + C₂H₆

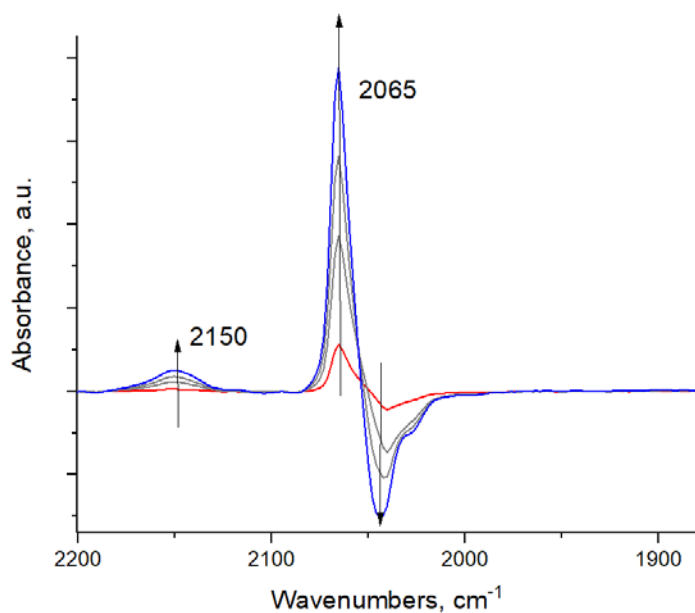


Figure S30. DRIFTS difference spectra (in time 1-5 minutes) during Ir(CO)(C₂D₄) during reaction with pure H₂ (H₂ flow ~10 cc/min). This shows clean selective conversion of Ir(I)(CO)(C₂D₄) to Ir(III)(CO)(H)₂. Unlike Rh(III)(CO)(H)_x/FAU which has a complex Rh-H band structure due to the formation of families of rhodium carbonyl hydride complexes with undissociated and dissociated hydrogen ligands Rh(I)(CO)(H₂) and Rh(III)(CO)(H)₂ in FAU micropores (see references 17 and 18 in the main text), the Ir sample shows clean conversion to Ir(III)(CO)(H)₂

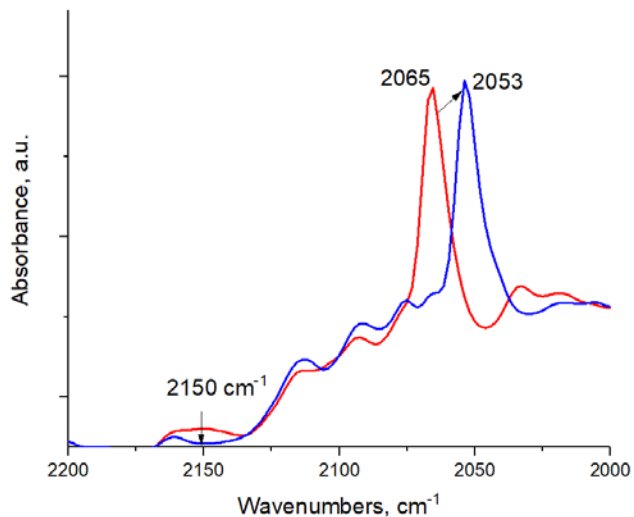


Figure S31. DRIFTS in time (2 minutes) during Ir(III)(CO)H₂ reaction with D₂. The following reaction takes place: Ir(III)(CO)(H)₂ + D₂ → Ir(III)(CO)(D)₂ + H₂; this fully confirms our assignment of 2150 cm⁻¹ band to the Ir-H stretch, it disappears due to the formation of the Ir-D bond.

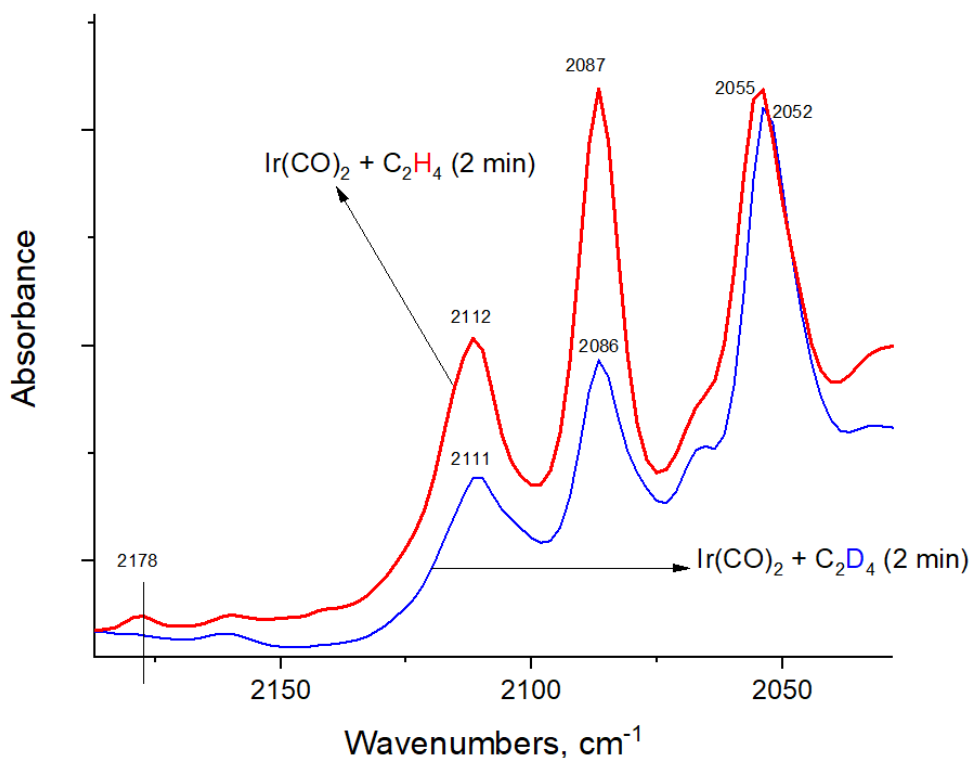


Figure S32. Comparison of DRIFTS spectra after the first 2 minutes of [Ir(CO)₂/FAU + C₂H₄] reaction (red spectrum) and [Ir(CO)₂/FAU + C₂D₄] reaction (blue spectrum). Note, that the 2,178 cm⁻¹ Ir-H band is absent in the C₂D₄ treated spectrum, confirming it is not a CO vibration but Ir-H vibration.

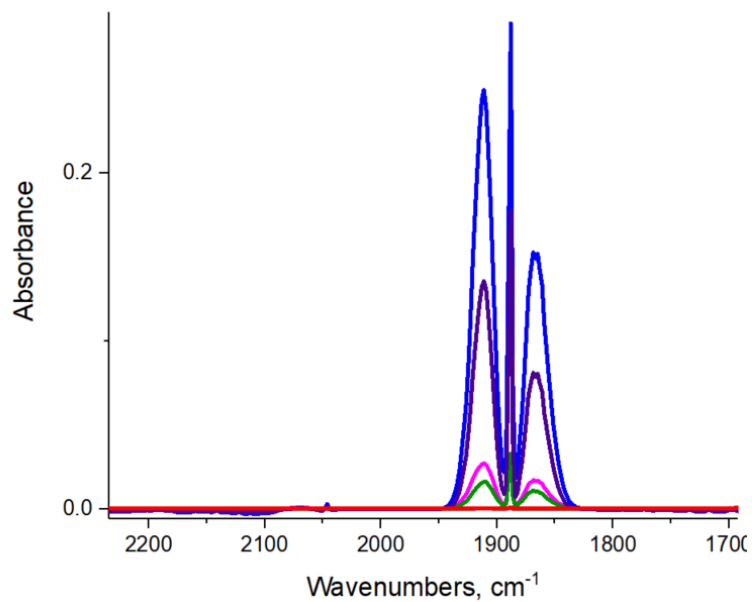


Figure S33. DRIFTS spectra during ethylene interaction Ni/BEA, showing no discernible features that could be attributed to Ni-H species. Dehydrated Ni/BEA sample was used as a background. Ethylene was flowed through the cell (blue spectrum in ethylene flow), we then purged ethylene with He continuously.